

Wavy regimes of film flow down a fibre

Christian Ruyer-Quil

FAST – UMR CNRS 7608, Université Pierre et Marie Curie (UPMC),

Campus universitaire, 91405 Orsay, France

Serafim Kalliadasis

Department of Chemical Engineering, Imperial College London,

London SW7 2AZ, United Kingdom

(Dated: October 10, 2011)

Abstract

We consider axisymmetric traveling waves propagating on the gravity-driven flow of a liquid down a vertical fibre. Our starting point is the two-equation model for the flow derived in the study by Ruyer-Quil *et al.* [*J. Fluid Mech.* **603**, 431 (2008)]. The speed, amplitude and shape of the traveling waves are obtained for a wide range of parameters by using asymptotic analysis and elements from dynamical systems theory. Four different regimes are identified corresponding to the predominance of four different physical effects: Advection by the flow, azimuthal curvature, inertia and viscous dispersion. Construction of the traveling-wave branches of solutions reveals complex transitions from one regime to another. A phase diagram of the different regimes in the parameter space is offered.

PACS numbers: 47.15.gm, 47.20.Ma, 47.35.Fg, 47.10.Fg

I. INTRODUCTION

A liquid film flowing down a vertical fibre is often encountered in a wide variety of technological applications such as condensers, emergency cooling of nuclear fuel rods and optical fibre coating. It can also serve as a simple prototype for the study of wave instabilities and transitions in open flow hydrodynamic and other nonlinear systems. As a consequence, this problem has been an active topic of both experimental and theoretical research, especially over the past two decades.

Experimental studies have revealed a complex wave dynamics dominated by axisymmetric and localised tear-drop-like structures which continuously interact with each other [1–5]. These structures are robust as they propagate over long distances without changing their speed or shape significantly; they are also separated by portions of nearly flat film, and they can be referred to as traveling waves. When the portions of nearly flat film between these structures are much longer than their characteristic length, the structures can be referred to as solitary waves. The formation of solitary/traveling waves results from the interplay between two different instability mechanisms: (i) The classical instability of a liquid film flowing down an inclined planar substrate prompted by inertia effects. This mode was initially characterised experimentally and theoretically by Kapitza and his son [6]; (ii) The interfacial instability of a liquid cylinder, considered first in experiments by Plateau and was theoretically explained by Lord Rayleigh [7, 8]. These two mechanisms are hereinafter referred to as the K and RP modes of instability, respectively.

The experimental study by Duprat *et al.* [5], in particular, provided reports on the traveling waves’ characteristics, namely shape, speed and amplitude, for very viscous fluids. The parameter values in the experiments were chosen in order to investigate the interplay of the K and RP modes on the waves; thus the study by Duprat *et al.* [5] completed the flow regime portrait obtained by Kliakhandler [2] for very viscous fluids but in the inertialess limit. Regular wavetrains were generated by means of a periodic forcing at the inlet. Two flow regimes were identified. For thin fibres and/or small flow rates, the RP mode is dominant and the solitary waves resemble beads or sliding drops whose shape is affected by gravity. In fact, when rescaled by the amplitude and the tail length, the profiles are nearly superimposed. At the same time, the flow field in a frame moving with the beads is characterised by recirculation zones within the beads. When closed streamlines exist in

the moving frame, a fluid particle is trapped in both moving and laboratory frames. Hence, the beads transport the trapped fluid mass downstream. For these reasons, we refer to the flow regime observed for thin fibres and/or small flow rates, as the *drop-like regime*.

For thick fibres and/or large flow rates, the K mode is dominant and a steepening of the wave front is observed with an increase of the wave amplitude. Mass transport is not observed in this regime except for a few cases corresponding to the largest waves. We refer to this regime as the *wave-like regime*. We can conjecture that the onset of recirculation zones in the wave-like regime is a signature of the increased prevalence of the K mode. Eventually, we observe a transition from the *drag-gravity* regime, where inertia plays a perturbative role, to the *drag-inertia* regime, where inertia effects become dominant. Similar regimes and a transition between the two as inertia effects increase were first observed in the planar case [9, 10].

Noteworthy is that the drop-like regime is similar to the one observed by Quéré [1] on a fibre or wire being pulled out from a liquid bath and results from the same physical mechanisms. The thin annular film that coats the wire can break up into drops. This drop formation process occurs when the typical time of growth of the RP instability is much smaller than the typical time of advection of a structure by the flow, i.e. for small fibre radii and/or small flow rates.

At the theoretical front, a number of modelling approaches have been proposed within the framework of the long-wave approximation of the Navier-Stokes equations and associated wall and free-surface boundary conditions [2, 3, 11–16]: The basic assumption of this approximation is that of slow spatial and time modulations of the film thickness motivating the introduction of a formal perturbation parameter, the ‘long-wave’ or ‘film parameter’ ϵ measuring such modulations. Perturbation expansions in terms of this parameter then lead to substantial simplifications of the governing equations and boundary conditions. Additional assumptions lead to further simplifications, i.e. small film thickness h in comparison to the fibre radius R or negligible inertia. The resulting models are either single evolution equations for the film thickness h , e.g. the model by Frenkel [11] based on the long-wave approximation only, or systems of two coupled evolution equations for the film thickness h and streamwise flow rate q which combine the long-wave approximation and other approaches, e.g. the model by Trifonov [12] based on the ‘integral-boundary-layer’ approximation and the more recent model by Novbari and Oron [16] based on an ‘energy integral’ method.

It should be noted that all the above studies neglected the second-order viscous terms originating from the stream-wise momentum equation (streamwise viscous diffusion) and tangential stress balance (second-order contributions to the tangential stress at the free surface). The recent study by Ruyer-Quil *et al.* [17] formulated a two-evolution equation model for h and q that took into account the second-order viscous terms but also included inertia and was not limited to small aspect ratios h/R . The model was based on a combination of the long-wave approximation and a weighted-residuals approach using appropriate polynomial test functions for the velocity field – a ‘weighted residuals integral boundary layer’ (WRIBL) model following the terminology introduced by Oron [18]. It should be noted that the WRIBL model is consistent [19] at $O(\epsilon)$ for the inertial terms and at $O(\epsilon^2)$ for the remaining contributions, whereas the models obtained by Trifonov [12] and Novbari and Oron [16] are not consistent at $O(\epsilon)$. Furthermore, the study by Duprat *et al.* [20] compared the wavetrains generated experimentally by periodic forcing at the inlet to the traveling-wave solutions of the WRIBL model showing remarkable agreement in all cases, thus validating experimentally the model. Experimental validation was done in the study by Ruyer-Quil *et al.* where the traveling-wave solutions of the WRIBL model were favorably compared to the experiments by Kliakhandler *et al.* [2] while the spatio-temporal dynamics of the film computed numerically with the WRIBL model was shown to be in good agreement with the experiments by Duprat *et al.* [4]

As was shown in [17], the second-order viscous terms have a dispersive effect on the speed of the linear waves (they introduce a wavenumber dependence on the speed) and hence we shall refer to this effect as *viscous dispersion*. Viscous dispersion influences the shape of the capillary ripples in front of a solitary hump, more specifically, the amplitude and frequency of the capillary ripples, an effect which is amplified as the Reynolds number is increased. Hence, viscous dispersion is in fact a linear effect, but interestingly it can have some crucial consequences on the nonlinear dynamics of the film and the wave-selection process in the spatio-temporal evolution. After all, solitary pulses interact through their tails which overlap, i.e. the capillary ripples and their amplitude and frequency will affect the separation distance between the pulses. For example, smaller-amplitude ripples will allow for more overlap between the tails of neighboring pulses, thus decreasing their separation distance. These points have been analyzed in detail in the recent work by Pradas *et al.* [21] on coherent structures interaction on falling films on planar substrates and the influence of

viscous dispersion on interaction. Their analysis was based on the weighted-residuals models obtained in [22–24].

The main aim of the present study is to characterize theoretically the solitary/traveling waves propagating down the fibre within the framework of the WRIBL model. A first stab to the investigation of the traveling wave solutions of the WRIBL model was the recent study by Ruyer-Quil *et al.* [17, Sect. 6]. In this study traveling wave solutions were constructed numerically and were favorably compared to the experiments by Kliakhandler *et al.* [2], as noted earlier. Here we undertake an asymptotic analysis of the governing equations for solitary/traveling waves in various limiting cases, i.e. in the limits of small/large values of the pertinent parameters. We also obtain both numerically and asymptotically static drops in the drop-like regime. Furthermore, by using elements from dynamical systems theory, we provide a detailed and systematic parametric study of their speed, shape and amplitude, i.e. we construct bifurcation diagrams for their speed as a function of pertinent parameters, as well as obtain ranges in the parameter space for which the K or RP modes of instability, prompted by inertia and azimuthal curvature, respectively, are dominant. We scrutinize the four different regimes described earlier (drop-like, wave-like, drag-gravity, drag-inertia), and provide detailed phase diagrams and corresponding regime maps for very viscous and less viscous fluids, thus providing a deeper understanding of the problem as well as new insights and also completing the flow regime diagram provided in [5] for viscous fluids.

Section II introduces the pertinent non-dimensionalization and the WRIBL model. Solitary wave solutions are constructed in § III. Asymptotic limits for small/large values of the pertinent parameters are analyzed in § IV. Traveling waves corresponding to the experimental conditions considered in [2, 4] are next discussed in § V. Section VI presents a phase diagram of the different regimes. Finally, a summary of our findings and concluding remarks are offered in § VII.

II. FORMULATION

A. Natural set of parameters

Consider a film flowing down a vertical cylinder under the action of gravity. The liquid has dynamic and kinematic viscosity, μ and ν , respectively, density ρ and surface tension

σ . The flow is assumed to remain axisymmetric. \bar{r} , \bar{x} , \bar{u} and \bar{t} denote the radial, pointing outwards from the fibre centreline coordinate, the axial coordinate oriented along gravity, the axial velocity distribution and time, respectively (bars are used to distinguish dimensional from dimensionless quantities unless the distinction is unnecessary). From simple physical considerations and without prior knowledge of the specific details of the system, the following scales can be readily identified: The fibre radius \bar{R} , the Nusselt thickness \bar{h}_N of the uniformly coated film, the length and time scales, $l_\nu = \nu^{2/3}g^{-1/3}$ and $t_\nu = \nu^{1/3}g^{-1/3}$, based on gravity and viscosity (making explicit the balance between gravity and viscous forces giving rise to the Nusselt flat-film solution) and the capillary length $l_c = \sqrt{\sigma/(\rho g)}$.

A first set of pertinent dimensionless groups arises from these scales. The aspect ratio

$$\tilde{\alpha} \equiv \bar{h}_N/\bar{R} \quad (1a)$$

which assesses azimuthal curvature effects at the scale of the film, the Goucher number [25],

$$Go \equiv \bar{R}/l_c, \quad (1b)$$

that compares azimuthal and axial surface tension effects and the Kapitza number,

$$\Gamma \equiv \sigma/(\rho\nu^{4/3}g^{1/3}) = (l_c/l_\nu)^2, \quad (1c)$$

comparing surface tension and viscosity. Useful combinations of these parameters are $h_N \equiv \bar{h}_N/l_\nu$ and \bar{h}_N/l_c . The former compares the film thickness to the gravity-viscous length scale and, indirectly, inertia and viscosity since the Nusselt base flow is the result of the balance of gravity and viscosity. The latter, \bar{h}_N/l_c is related to the Bond number $Bo = \rho g \bar{h}_N^2/\sigma = (\bar{h}_N/l_c)^2$ comparing surface tension and gravity at the scale of the film.

The advantage of the set of parameters $\tilde{\alpha}$, Go and Γ is that when the geometry and the working fluid are fixed, the Goucher and the Kapitza numbers Go and Γ are constant and the only free parameter is $\tilde{\alpha}$. From an experimental point of view, $\tilde{\alpha}$ can be varied independently by varying the inlet flow rate. The Kapitza number Γ is entirely defined by the fluid properties independently of the flow characteristics, whereas the Goucher number Go can be easily varied by replacing the fibre. Hence, the parameters $\tilde{\alpha}$, Go and Γ can therefore be viewed as ‘natural’ for the fibre problem, and we will systematically recast our results in terms of these parameters $\tilde{\alpha}$, Go and Γ .

Table I gives the physical properties of four different fluids of increasing viscosities commonly used in experiments and corresponding to a wide range of Kapitza numbers together

	ν (mm ² s ⁻¹)	ρ (kgm ⁻³)	σ (mNm ⁻¹)	l_c (mm)	l_ν (mm)	Γ
water	1	998	72.5	2.7	0.047	3376
Rhodorsil silicon oil v50	50	963	20.8	1.5	0.63	5.48
castor oil	440	961	31	1.8	2.7	0.45
Rhodorsil silicon oil v1000	1000	980	21.1	1.5	4.7	0.10

TABLE I. Fluid properties, capillary length l_c , gravity-viscous length l_ν and Kapitza number used in the present study. The data for silicon oil v50 and castor oil have been taken from [2, 4].

with the corresponding capillary lengths and viscous-gravity length scales. For simplicity, our results will be presented for the Kapitza numbers listed in table I.

B. WRIBL model

We now adapt Shkadov's scaling [26] and introduce different length scales for the streamwise (axial) and radial directions. The length scale in the radial direction is the Nusselt thickness \bar{h}_N , whereas the length scale in the streamwise direction is chosen as $\kappa\bar{h}_N$ defined by the balance of the streamwise pressure gradient induced by capillarity, $\propto \sigma\partial_{xxx}h$, and gravity acceleration, ρg , which gives $\kappa = [\sigma/(\rho g\bar{h}_N^2)]^{1/3} = (l_c/\bar{h}_N)^{2/3}$. The time scale is defined with reference to the Nusselt solution of uniform thickness (a result of the balance of gravity and viscosity). The volumetric flow rate per unit length of circumference, $q_N = R^{-1} \int_R^{R+h_N} u r dr$, of a film of constant thickness \bar{h}_N is given by

$$\bar{q}_N \equiv \frac{g\bar{h}_N^3}{3\nu} \phi(\tilde{\alpha}), \quad (2)$$

where ϕ is a geometric factor defined in (A1a) and measures the deviation of the flow-rate-to-thickness relation from the cubic dependency corresponding to the planar geometry ($\phi(0) = 1$). Similarly to the streamwise length scale, the time scale is stretched by a factor κ and thus defined as $3\kappa\bar{h}_N^2/\bar{q}_N = \nu\kappa/[g\bar{h}_N\phi(\tilde{\alpha})]$.

Our basic equations for the analysis to follow are the WRIBL model obtained in [17], a set of two evolution equations for the local film thickness $h(x, t)$ and the local flow rate $q(x, t) \equiv R^{-1} \int_R^{R+h(x,t)} u r dr$. For the sake of clarity and completeness we re-write the WRIBL

model here,

$$\partial_t h = -\frac{1}{1 + \tilde{\alpha}h} \partial_x q, \quad (3a)$$

$$\begin{aligned} \delta \partial_t q = & \delta \left[-F(\tilde{\alpha}h) \frac{q}{h} \partial_x q + G(\tilde{\alpha}h) \frac{q^2}{h^2} \partial_x h \right] + \frac{I(\tilde{\alpha}h)}{\phi(\tilde{\alpha})} \left[-\frac{3\phi(\tilde{\alpha})}{\phi(\tilde{\alpha}h)} \frac{q}{h^2} \right. \\ & \left. + h \left\{ 1 + \partial_{xxx} h + \frac{\beta}{(1 + \tilde{\alpha}h)^2} \partial_x h - \frac{1}{2} \partial_x \left(\frac{\tilde{\alpha}}{1 + \tilde{\alpha}h} (\partial_x h)^2 \right) \right\} \right] \\ & + \eta \left[J(\tilde{\alpha}h) \frac{q}{h^2} (\partial_x h)^2 - K(\tilde{\alpha}h) \frac{\partial_x q \partial_x h}{h} - L(\tilde{\alpha}h) \frac{q}{h} \partial_{xx} h + M(\tilde{\alpha}h) \partial_{xx} q \right], \quad (3b) \end{aligned}$$

in terms of the Shkadov scaling, where ϕ , F , G , I , J , K , L , and M are functions of the aspect ratio $\tilde{\alpha}$ given in Appendix A. Equation (3a) is the (exact) dimensionless mass balance whereas (3b) is the streamwise momentum equation averaged across the film with a weighted-residuals approach. It should be emphasized that the WRIBL model has been validated in [5, 17] through direct comparisons to the experiments in [2, 4, 5] as noted in § I [for both very viscous and less viscous liquids (castor oil and silicon oil V50, see table I) and a wide range of the parameters ($0.15 \leq Go \leq 1$ and $0.5 \leq \tilde{\alpha} \leq 4.5$)].

Shkadov's scales introduce three new dimensionless groups besides the aspect ratio $\tilde{\alpha} = h_N/R$, a 'reduced Reynolds number',

$$\delta \equiv 3\bar{q}_N/(\nu\kappa) = (\tilde{\alpha}Go)^{11/3} \phi(\tilde{\alpha})\Gamma^{3/2}, \quad (4a)$$

which compares inertia and the viscous drag at the scale $\kappa\bar{h}_N$ introduced by the balance of gravity and capillarity, a streamwise 'viscous dispersion parameter',

$$\eta \equiv 1/\kappa^2 = (\bar{h}_N/l_c)^{4/3} = (\tilde{\alpha}Go)^{4/3}, \quad (4b)$$

and the dimensionless group,

$$\beta \equiv \tilde{\alpha}^2/\eta = \tilde{\alpha}^{2/3}Go^{-4/3}, \quad (4c)$$

which is a combination of $\tilde{\alpha}$ and η and compares azimuthal to axial surface tension effects. We have made explicit in (4) the relations of δ , η and β to the 'natural' parameters $\tilde{\alpha}$, Go and Γ . Notice that all second-order/viscous-dispersion terms are gathered in the last row of (3b) and are multiplied by η . Finally, we recall the usual definition of the Reynolds number based on the flow rate, $Re = \bar{q}_N/\nu = h_N^3\phi(\tilde{\alpha})/3$ where again $h_N = \bar{h}_N/l_\nu$.

The advantage of Shkadov's scaling stems from (i) the direct reference to the Nusselt uniform film flow that simplifies the comparisons between solutions, with the Nusselt solution

corresponding to constant values of the film thickness and flow rates $h = 1$ and $q = 1/3$; (ii) the association of a single parameter to each physical effect affecting the balance of the different forces: Inertia (δ), azimuthal surface tension (β), viscous dispersion (η) and geometry ($\tilde{\alpha}$).

As noted in § I the WRIBL model was derived with the long-wave approximation (i.e. under the assumption of slow space and time modulations, $\partial_{x,t} \sim \epsilon$, where ϵ is the long-wave/film parameter) and a weighted-residuals approach in which the velocity field is expanded on an appropriately chosen set of test functions. This expansion takes into account the (small) deviations of the velocity field from the uniform-thickness solution. As also noted in § I, contrary to the model obtained by Trifonov [12] – see also [27] – and to the model by Novbari and Oron [16], (3) is consistent up to $O(\epsilon)$ for the inertia terms and up to $O(\epsilon^2)$ for the remaining contributions (and accounts for viscous dispersion). Indeed, both Trifonov’s and Novbari and Oron’s approaches assume a self-similar velocity distribution and do not account for the deviations of the velocity profile induced by the free-surface deformations. For this reason, their two-equation formulations lack consistency even at first order in the film parameter. Furthermore, we note that the energy-integral approach employed by Novbari and Oron [16] is not consistent with the kinetic energy balance of the flow. Indeed, writing formally the axial momentum equation as $\mathcal{M}(u) = 0$, Novbari and Oron’s averaged momentum equation reads $\int_R^{R+h} \mathcal{M}(u)u \, dr = 0$ whereas the kinetic energy balance of a section of the liquid corresponds to $\int_R^{R+h} \mathcal{M}(u)u \, d(r^2) = 0$. Truncating then $\mathcal{M}(u)$ at $O(\epsilon^2)$ is equivalent to the Galerkin approach that can be used to reduce the algebra leading to (3b) [17]. Noteworthy is that the two-equation model (3) is not limited to small aspect ratios unlike, e.g. the model by Roberts and Li [15].

To end this section let us point out one apparent drawback of the Shkadov scaling, namely the divergence of the dimensionless parameter $\beta = \tilde{\alpha}^2/\eta$ as the viscous dispersion parameter goes to zero for $\tilde{\alpha} = O(1)$. The divergence of β signals that the typical length of a wave is not determined by the balance of gravitational and axial capillary forces, as assumed in Shkadov’s scaling, but rather by the balance of axial and azimuthal capillary forces, in which case the typical curvatures of the beads in the azimuthal and axial directions must coincide. The beads have thus a drop-like rounded shape, the long-wave approximation starts to be violated and the viscous dispersion effects cannot be a priori discarded as in the planar case. Considering drop-like beads (see §-IV A) it can thus be useful to adopt a scaling based on

the radius \bar{R} of the fibre, which gives the time scale $\nu/(g\bar{R})$. This scaling introduces a Galilei number, $Ga \equiv g\bar{R}^3/\nu^2 = Go^3\Gamma^{3/2}$.

C. Surface equations and saturation numbers

Neglecting inertia and viscous dispersion, Craster and Matar [3] formulated a single evolution equation for the film thickness h , the Craster and Matar (CM) equation,

$$\partial_t \left(h + \frac{\tilde{\alpha}}{2} h^2 \right) + \partial_x \left[\frac{h^3}{3} \frac{\phi(\tilde{\alpha}h)}{\phi(\tilde{\alpha})} \left(1 + \frac{\beta}{(1 + \tilde{\alpha}h)^2} \partial_x h + \partial_{xxx} h \right) \right] = 0. \quad (5)$$

For sufficiently thin films, that is $\tilde{\alpha} \rightarrow 0$, we obtain from (5)

$$\partial_t h + \partial_x \left[\frac{h^3}{3} (1 + \beta \partial_x h + \partial_{xxx} h) \right] = 0, \quad (6)$$

which is the equation derived initially by Frenkel [11] (see also [13]). Equations (5) and (6) are the simplest evolution equations balancing all relevant physical effects, gravity, viscous drag, surface tension and the fibre curvature. They are equations for the free surface $h(x, t)$ only and following the terminology introduced by Ooshida [9], we shall refer to them as *surface equations*.

The CM equation offers a simple prototype for the flow, easily amenable to mathematical and numerical scrutiny. It can be obtained asymptotically from (3) in the limit $\delta \rightarrow 0$ and $\eta \rightarrow 0$ when the nonlinear term $-1/2\partial_x(\tilde{\alpha}/(1 + \tilde{\alpha}h)(\partial_x h)^2)$ of the azimuthal curvature gradient is omitted. Yet, as already stated, $\tilde{\alpha} = O(1)$ implies that β diverges to infinity and therefore that second-order viscous dispersive terms cannot be a priori discarded and that the long-wave assumption is invalid. By contrast, the derivation of the Frenkel's equation (6) can be obtained in the distinguished limit $\tilde{\alpha} \rightarrow 0$, $\eta \rightarrow 0$ and $\beta = \tilde{\alpha}^2/\eta = O(1)$. Nevertheless, comparisons of the solutions to the CM equation to the experiments show good agreement [17, 20].

Using the surface equation (6), Kalliadasis and Chang [13], and Chang and Demekhin [28] analysed the mechanism of the formation of drops observed by Qy  r   [1] when a fibre or wire is drawn out of a liquid bath. Q  r   observed suppression of the RP mode for sufficiently small coating films. More specifically, below a certain critical thickness the film deposited on the wire develops small-amplitude interfacial waves with the flow preventing their growth into drops (such drops would always be observed when the wire is horizontal, as the suppression of the RP mode induced by the flow is absent in this case). On the other hand,

beyond the critical film thickness growth of the interfacial waves into drops was observed. Kalliadasis and Chang [13] found that the amplitude of the solitary-wave solutions to (6) diverges/‘blows-up’ for β larger than a critical value $\beta_c = 1.413$, which closely corresponds to the formation of drops in Quéré’s experiments. These authors also performed an analytical construction of the solitary waves for $\beta \rightarrow \beta_c$ using matched asymptotic expansions. They showed that drop formation results from the inability of the flow advection to saturate the instability growth through a nonlinear saturation mechanism.

The advection and the growth of the instability can be compared through the definition of the advection time τ_a of an interfacial structure over its length and the definition of a typical time of growth of the structure τ_g as the inverse of the maximum growth rate. Based on the Finkel equation (6), the stability analysis of the uniform film leads to the dispersion relation

$$\omega = k + \frac{ik^2}{3}(\beta - k^2) \quad (7)$$

which governs infinitesimal perturbations around the base Nusselt flow of wavenumber k and angular frequency ω . Based on (7) the ratio τ_a/τ_g reads:

$$\tau_a/\tau_g = \omega_i/\omega_r|_{k=\sqrt{\beta/2}} \propto \beta^{3/2} \quad (8)$$

(see [17] for details). Therefore, β compares τ_a to τ_g . For, $\beta < \beta_c$, the instability growth is slower and thwarted than the advection by the flow. The same mechanism is also in play in the saturation of the drops though it is then strongly nonlinear. For these reasons, we refer to β as a *saturation number*, a term that was first introduced in [5].

From the CM equation (5), we get $\tau_a/\tau_g \propto (\beta^*)^{3/2}$ where the composite parameter β^* is defined as [4, 17]:

$$\beta^* = \beta c_k^{-2/3} (1 + \tilde{\alpha})^{-8/3}. \quad (9)$$

c_k is the speed at which infinitesimal deformations of the free surface are kinematically transported by the flow, or *kinematic wave speed*:

$$c_k = \frac{1}{1 + \tilde{\alpha}} \left[1 + \frac{\tilde{\alpha}\phi'(\tilde{\alpha})}{3\phi(\tilde{\alpha})} \right] = \frac{8(b-1)(2\log(b)b^2 - b^2 + 1)}{3(4\log(b)b^4 - 3b^4 + 4b^2 - 1)}, \quad (10)$$

with $b = 1 + \tilde{\alpha}$.

Since $c_k(\tilde{\alpha} = 0) = 1$, $\lim_{\tilde{\alpha} \rightarrow 0} \beta^* = \beta$. In this limit the Frenkel equation (6) limited to very thin films ($\tilde{\alpha} \ll 1$) applies and β^* is a generalisation of the saturation number β to film flows with thicknesses comparable to the fibre radius.

III. SOLITARY WAVES AND DYNAMICAL SYSTEMS THEORY

Experimental studies [2–5] reported the formation of axisymmetric traveling waves (TWs) propagating without deformations and at constant speed over long distances. Solitary waves, i.e. TWs separated by constant-thickness layers of fluid, or substrates, much longer than the characteristic length of the waves, were commonly observed sufficiently far downstream. Theoretically, solitary waves can be viewed as periodic TWs with an infinitely long wavelength. The aim of this section is to investigate infinite-domain solitary waves using elements from dynamical systems theory.

In a frame of reference moving with the speed c of the waves, $\xi = x - ct$, the flow is stationary and the set of partial differential equations (3) can be converted into a set of ordinary differential ones. The mass balance (3a) can be integrated once,

$$q - c \left(h + \frac{\tilde{\alpha}}{2} h^2 \right) \equiv q_0, \quad (11)$$

where q_0 is the rate at which the fluid flows under the waves. The averaged momentum balance (3b) next reads,

$$\begin{aligned} & \delta \left[c q' - F(\tilde{\alpha} h) \frac{q}{h} q' + G(\tilde{\alpha} h) \frac{q^2}{h^2} h' \right] + \frac{I(\tilde{\alpha} h)}{\phi(\tilde{\alpha})} \left[-\frac{3\phi(\tilde{\alpha})}{\phi(\tilde{\alpha} h)} \frac{q}{h^2} \right. \\ & + h \left\{ 1 + h''' + \frac{\beta}{(1 + \tilde{\alpha} h)^2} h' + \frac{\tilde{\alpha}}{1 + \tilde{\alpha} h} h' \left[h'' - \frac{1}{2} \frac{\tilde{\alpha}}{1 + \tilde{\alpha} h} (h')^2 \right] \right\} \Bigg] \\ & + \eta \left[J(\tilde{\alpha} h) \frac{q}{h^2} (h')^2 - K(\tilde{\alpha} h) \frac{q' h'}{h} - L(\tilde{\alpha} h) \frac{q}{h} h'' + M(\tilde{\alpha} h) q'' \right] = 0, \end{aligned} \quad (12)$$

where the primes denote differentiation with respect to the moving coordinate ξ . Using (11), (12) can be recast into $h''' = f(h, h', h'')$, where f is a function of the thickness h , its first and second derivatives and the parameters δ , $\tilde{\alpha}$, η and c . We thus end up with a dynamical system of dimension three,

$$\frac{d}{d\xi} \mathbf{U} = (U_2, U_3, f(U_1, U_2, U_3))^t, \quad (13)$$

where $\mathbf{U} = (U_1, U_2, U_3)^t \equiv (h, h', h'')$.

Solitary waves correspond to homoclinic orbits in the phase space connecting a fixed point to itself. Here we restrict our attention to single-loop homoclinic orbits corresponding to single-hump solitary waves in real space. The fixed points of the dynamical system (13) satisfy $h' = h'' = 0$ and,

$$\frac{h^3}{3} \frac{\phi(\tilde{\alpha} h)}{\phi(\tilde{\alpha})} - c \left(h + \frac{\tilde{\alpha}}{2} h^2 \right) = q_0. \quad (14)$$

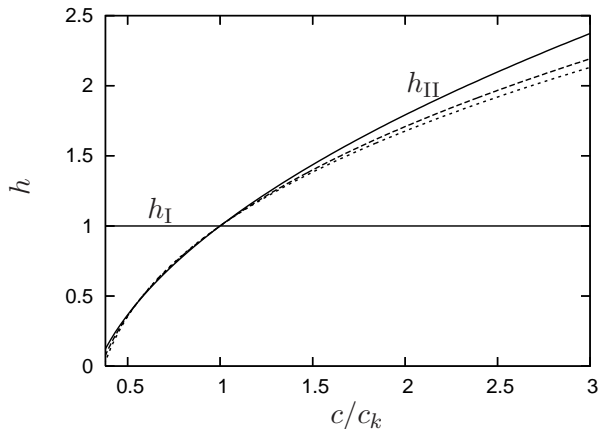


FIG. 1. Film thicknesses $h_I = 1$ and h_{II} corresponding to the location of the fixed points as function of the ratio of the normalised wave speed c to the kinematic wave speed c_k defined in (10). Solid, dashed and dotted lines refer to $\tilde{\alpha} = 0$ (planar case), $\tilde{\alpha} = 0.5$ and $\tilde{\alpha} = 1$, respectively.

Requiring that $h = 1$ is a solution to (14) gives:

$$q_0 = \frac{1}{3} - c \left(1 + \frac{\tilde{\alpha}}{2} \right). \quad (15)$$

In addition to the solution $h = 1$, there is one more real positive solution to (14) with (15) and the dynamical system (13) admits two fixed points $\mathbf{U}_I = (1, 0, 0)^t$ and $\mathbf{U}_{II} = (h_{II}, 0, 0)^t$ whose positions are displayed in Fig. 1 as functions of the wave speed c and aspect ratio $\tilde{\alpha}$. The two fixed points coincide when the wave speed c is equal to the speed of linear waves of infinitesimal amplitude and infinite length that are neutrally stable. This situation corresponds to the definition of the linear kinematic waves in the zero-wavenumber limit, whose speed is given in (10). In the limit $\tilde{\alpha} = 0$, we recover the expression $h_{II} = -1/2 + \sqrt{3(c - 1/4)}$ corresponding to a film flowing down an inclined plane [10, 29]. We note that extending this expression to the axisymmetric geometry by replacing c with c/c_k , gives a reasonable approximation $h_{II} \approx -1/2 + \sqrt{3[(c/c_k) - 1/4]}$ for the position of the second fixed point even for $\tilde{\alpha} = O(1)$ (see Fig. 1). Finally, we note that it is sufficient to consider homoclinic orbits around only one of the two fixed points because of the presence of a continuous family of Nusselt flat-film solutions parameterized by the reduced Reynolds number δ (or $h_N = \bar{h}_N/l_\nu$) when Go and Γ are held constant. Indeed, homoclinic orbits connecting \mathbf{U}_{II} correspond to phase-space trajectories connecting \mathbf{U}_I through the transformation $h_N \rightarrow h_N h_{II}$.

The shape of the tail and front of a solitary wave can be determined by considering how

the corresponding homoclinic orbit in the phase space approaches and leaves the fixed point it connects to. Let us consider the linear stability of the fixed point \mathbf{U}_I . The dispersion relation governing infinitesimal perturbations $\sim \exp(\lambda\xi)$ is

$$\lambda^3 + \lambda^2 \eta D_\eta + \lambda \delta D_\delta - 3(1 + \tilde{\alpha})(c - c_k) = 0, \quad (16)$$

where

$$D_\eta = \frac{\phi}{I} \left[-\frac{L}{3} + c(1 + \tilde{\alpha})M \right] \quad \text{and} \quad D_\delta = \left\{ \frac{\phi}{I} \left[(1 + \tilde{\alpha}) \left(c^2 - \frac{F}{3}c \right) + \frac{G}{9} \right] + \frac{\beta}{\delta(1 + \tilde{\alpha})^2} \right\}. \quad (17)$$

Equation (16) can be reduced to the canonical form $P(y) = y^3 + py + q = 0$ by the change of variable $\lambda = y - \eta D_\eta/3$, where

$$p = \delta D_\delta - \frac{\eta^2 D_\eta^2}{3} \quad \text{and} \quad q = -3(1 + \tilde{\alpha})(c - c_k) - \frac{\delta \eta}{3} D_\delta D_\eta + \frac{2\eta^3}{27} D_\eta^3. \quad (18)$$

Using the Cardan formulae, (16) admits a real eigenvalue and a complex conjugate pair when the discriminant $\Delta = 4p^3 + 27q^2$ is > 0 . When $\Delta < 0$, (16) admits three real eigenvalues. Therefore \mathbf{U}_I changes from a saddle to a saddle-focus at $\Delta = 0$. When \mathbf{U}_I is a saddle, the homoclinic orbit departs and returns to the fixed point monotonically along the two eigenspaces corresponding to the eigenvalues of smallest absolute value, and the corresponding tail and front of the solitary wave are monotonic. Conversely, when \mathbf{U}_I is a saddle-focus, the homoclinic orbit leaves monotonically along the eigenspace spanned by the eigenvector corresponding to the real eigenvalue and returns to the fixed point by spiralling on the eigenspace spanned by the eigenvectors corresponding to the complex pair. This spiral corresponds to capillary ripples at the front of the solitary wave while the tail remains monotonic.

Figure 2 displays the speed and maximum amplitude of the solitary waves corresponding to homoclinic orbits around $\mathbf{U}_I = (1, 0, 0)^t$. Parameters correspond to the fluid properties of silicon oil v50 ($\Gamma = 5.48$, see table I) and to different fibre radii, $R = 1.5$ mm, 0.35 mm and 0.25 mm ($Go = 1, 0.24$ and 0.17). The solutions have been computed by continuation using AUTO97 together with its subroutine HOMCONT [30]. In all cases $\Delta > 0$, i.e. \mathbf{U}_I is a saddle-focus and the solitary waves are characterised by monotonic tails and oscillatory fronts.

Two different behaviours can be observed for small and large thicknesses, or for $\delta \ll 1$ and $\delta \gg 1$. [31] For small thicknesses ($\delta \ll 1$), the maximum height h_{\max} and speed of the

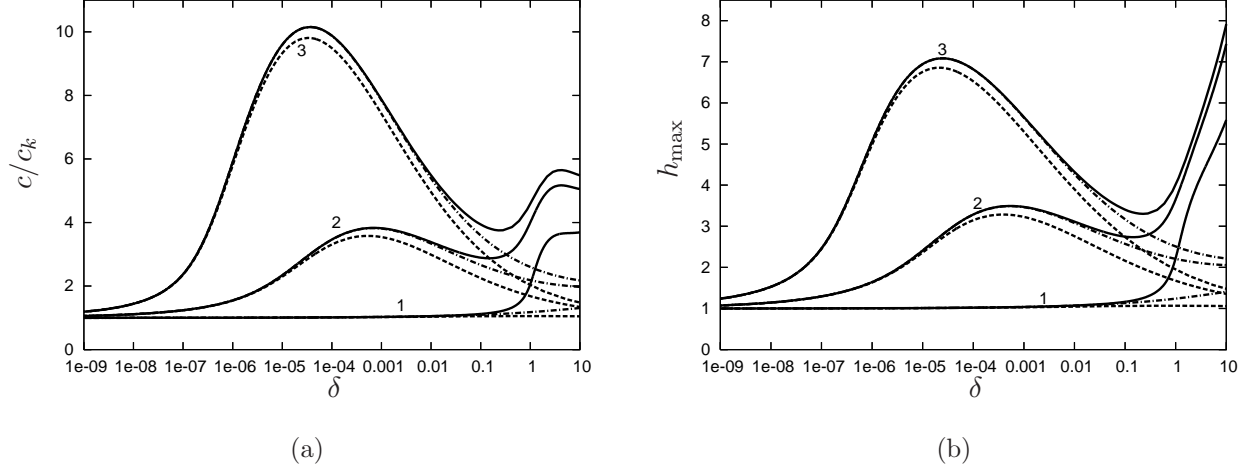


FIG. 2. Speed c (left) and maximum height h_{\max} (right) of the solitary waves as function of the reduced Reynolds number δ for different fibre radii: $R = 1.5$ mm (Curves 1), 0.35 mm (2) and 0.25 mm (3). Solutions to (3) (solid lines) are compared to the solutions of the CM equation (5) and of the model (3) when inertial terms are set to zero (dashed and dashed-dotted lines). The fluid properties correspond to Rhodorsil silicon oil v50 (see table I).

solitary waves exhibit local maxima which strongly increase for thin fibres corresponding to a stronger RP instability. In Figs. 2(a) and 2(b), the characteristics of the solitary wave solutions of the WRIBL model (3) and of the CM equation (5) are compared showing reasonable agreement. As the CM equation is parameterized by the aspect ratio $\tilde{\alpha}$ and β , the local maxima are the result of the balance of curvature effects and the advection by the flow. This is reminiscent of the sharp increase, or ‘blow-up’, of speed and amplitude observed by Kalliadasis and Chang [13] at $\beta = \beta_c \approx 1.413$ in their study of the solitary wave solutions of the Frenkel equation (6).

One might expect that the sharp increase of the local maxima of the speed and amplitude observed by lowering the fibre radius is related to the nonlinear saturation mechanism of the instability by the advection discussed earlier and, therefore, it should be correlated with the saturation number β^* . The validity of this hypothesis is checked in Fig. 3 where the maximum height of the solitary waves is depicted as a function of β^* . At a given value of the Goucher number Go , β^* reaches a maximum for $\tilde{\alpha} \approx 0.44$ and tends to zero for $\tilde{\alpha} \rightarrow 0$ and $\tilde{\alpha} \rightarrow \infty$. For a fixed radius R , δ and $\tilde{\alpha}$ have the same trend. This explains why β^* tends to zero when $\delta \rightarrow 0$ and $\delta \rightarrow \infty$ and justifies the shapes of the curves. The local maximum

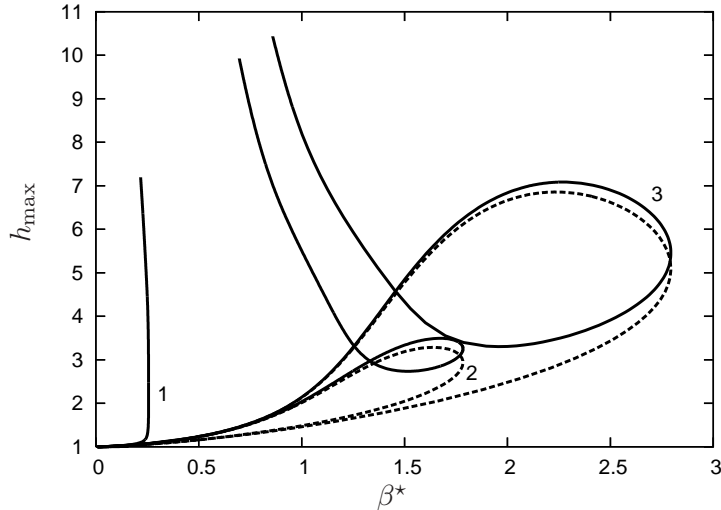


FIG. 3. Maximum height of solitary waves versus saturation parameter β^* . See also caption of Fig. 2.

of h_{\max} occurs at β^* close to the maximum reached by this parameter as δ is varied. The increase of the local maximum of h_{\max} is related to the increase of the maximal value of β^* achieved as the ratio Go is lowered.

We have also computed solutions of model (3) when the inertial terms are cancelled ($\delta \rightarrow 0$). The results are shown as dashed-dotted lines in Figs. 2(a) and 2(b). As they asymptote to the solid lines corresponding to (3) in the limit $\delta \ll 1$, we can conclude that the difference in speed and amplitude between solutions to (3) and to the CM equation result from the viscous dispersion effects that contribute to the increase of the speed and amplitude of the solitary waves.

Figure 2 reveals a sharp increase of the maximum height and speed of the waves above $\delta \approx 2$ corresponding to the predominance of the K mode (as the planar case is approached, i.e. when the fibre radius increases, this sharp increase corresponds precisely to the transition between the drag-gravity and drag-inertia regimes). The characteristics of the waves in this region will be considered in detail later on in §IV B. The separation between the local maxima for the speed and amplitude corresponding to the RP-dominated waves ($\delta \ll 1$) and the K-dominated waves at large δ increases for even more viscous fluids like the castor oil used by Kliakhandler [2] (cf. Table I) as can be observed from Fig. 4(b) where the solutions of the model (3) with and without inertia, and of the CM equation are compared

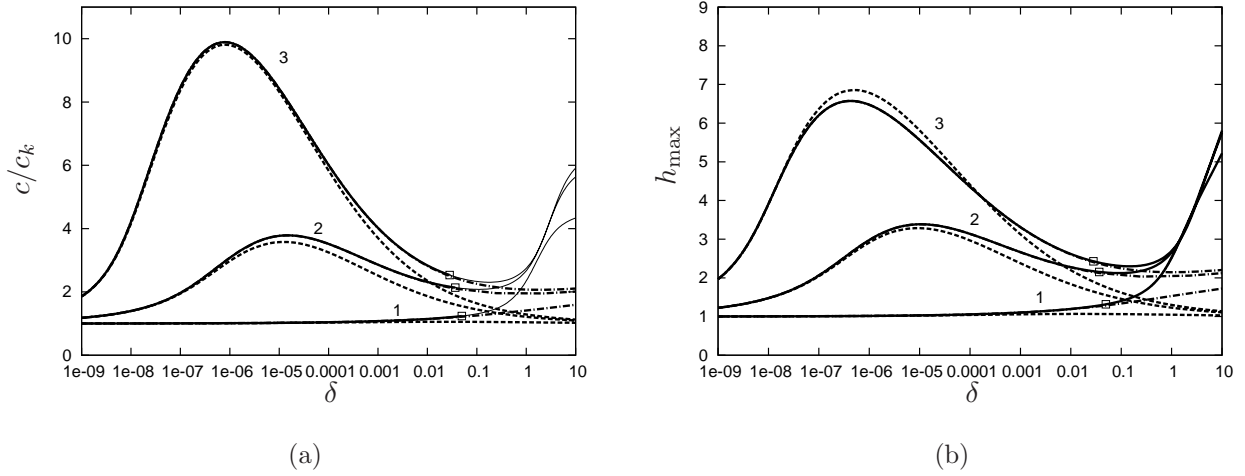


FIG. 4. Speed c (left) and maximum height h_{\max} (right) as function of the reduced Reynolds number δ for different fibre radii: $R = 1.83$ mm (Curves 1), 0.43 mm (2) and 0.31 mm (3). Solutions to (3) (solid lines) are compared to the solutions of the CM equation (5) and of the model (3) when inertial terms are set to zero (dashed and dashed-dotted lines). Homoclinic orbits connecting a saddle-focus (saddle) fixed point to itself are shown in thick (thin) solid lines. Squares indicate the loci of saddle to saddle-focus transitions. The fluid properties correspond to castor oil ($\Gamma = 0.45$).

for fibre radii corresponding to the same ratios $Go = 1, 0.24$ and 0.17 as in figure 2. This increase can be understood by considering the definition of β^* , which is a function of the aspect ratio $\tilde{\alpha}$ and Go , and the definition of $\delta = (\tilde{\alpha}Go)^{11/3}\phi(\tilde{\alpha})\Gamma^{3/2}$. Since the Kapitza number Γ decreases with the kinematic viscosity, the maximum of β^* for a given value of the Goucher number Go corresponds to smaller and smaller values of the reduced Reynolds number δ as the viscosity of the fluid is increased. In contrast with the results for silicon oil v50 (cf. Fig. 2), a transition from a saddle-focus to a saddle fixed point has been observed corresponding to the disappearance of the capillary ripples at the front of the solitary wave at values of δ above 0.1 . The precise location of this transition varies with the fibre radius R and is indicated by squares in figure 4(a).

Conversely, the separation of the solitary wave characteristics, such as speed and maximum height, as a function of δ into two distinct regions, at low and high reduced Reynolds numbers, vanishes at low viscosities. Indeed at low viscosities, or equivalently, high Kapitza numbers, the RP mode occurs at relatively high values of δ where the K mode already takes

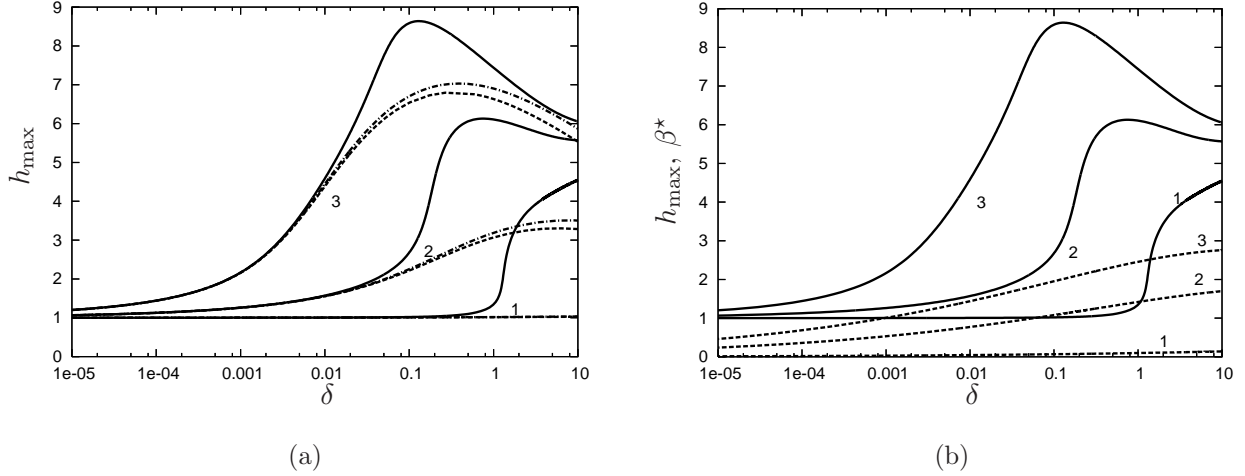


FIG. 5. (a) Maximum height h_{\max} of the solitary waves as function of δ . Solutions of (3) (solid lines) are compared to the solutions of the CM equation (5) (dashed lines) and solutions of (3) where the inertia terms are set to zero (dashed-dotted lines). (b) Maximum height h_{\max} (solid line) and parameter β^* (dashed lines). Parameters correspond to water ($\Gamma = 3376$) and different fibre radii: $R = 2.75$ mm (Curves 1), 0.64 mm (2) and 0.46 mm (3).

over. In Fig. 5(a) we have redrawn Fig. 2(b) for water ($\Gamma = 3376$, see Table I), which is fifty times less viscous than silicon oil v50. The figure compares the maximum height of the solitary waves for a ratio of the Goucher number Go equal to the ones chosen for the computations shown in Figs. 2, to the amplitude of the solutions of the CM equation (5). At small values of δ , the amplitude of the waves is significantly larger than the amplitude of the solutions of the CM equation, which signals the influence of the K mode on the RP instability. Notice that this effect cannot arise from the second-order viscous terms as the cancellation of the inertial terms leads to results comparable to the solutions of the CM equation. On the other hand, the influence of the RP instability on the K mode is illustrated in Fig. 5(b) where β^* and h_{\max} are plotted versus δ . At small fibre radii $R = 0.64$ mm and $R = 0.46$ mm ($Go = 0.24$ and 0.17), the characteristic sharp increase of the solitary-wave amplitude is displaced to values of δ smaller than $\delta \approx 2$ corresponding to a generalised saturation number $\beta^* \gtrsim 1$.

Go	$\tilde{\alpha}$	h_{\max}	c	\bar{h}_{\max}/\bar{R}	$c\nu/(g\bar{R}^2)$	$c_{\text{drops}}\nu/(g\bar{R}^2)$
0.236	0.23	3.3	3.1	0.77	0.22	0.25
0.168	0.15	6.9	8.8	1.05	0.25	0.30
0.110	0.075	18	38.5	1.36	0.24	0.29
0.055	0.022	81.2	383	1.80	0.19	0.22
0.044	0.014	129	773	1.85	0.16	0.18

TABLE II. Local maxima of the speed c and amplitude h_{\max} with respect to δ for given values of the Goucher number Go , or equivalently $\tilde{\alpha}$, obtained from the CM equation (5). c_{drops} refers to the speed of quasi-static drops sliding downwards coated fibres (see text and Appendix B).

IV. LIMITING CASES

In this section, we focus on the different regions of the wave-characteristics' diagrams displayed in Figs. 2, 4 and 5, and consider all possible asymptotic limits.

A. Small Goucher number limit: the drop-like regime

Let us first consider the local maxima of the amplitude h_{\max} and speed c with respect to δ for given values of the Goucher number Go , or equivalently $\tilde{\alpha}$, observed for viscous fluids like silicon oils in the inertia-less limit ($\delta \ll 1$). Table II depicts these quantities as obtained from the CM equation. As Go tends to zero, the RP instability mechanism becomes more and more efficient and we observe a sharp increase of the local maxima of the amplitude h_{\max} and of the maxima of the speed of the waves. For such waves, the amplitude can be several orders of magnitude larger than the Nusselt flat film on which they stand, and variations of the Nusselt thickness should only slightly modify the wave characteristics (except perhaps when the film becomes so thin that the corner dissipation at the wave front dominates over the dissipation in the bulk).

Since $\bar{R} \ll l_c$, azimuthal surface tension effects dominate over gravity and the typical length scale and height of a wave should correspond to the radius \bar{R} of the fibre as already pointed out in § II B. The wave speed should then be determined by the balance of viscosity and gravity at the scale \bar{R} which gives a typical velocity of $g\bar{R}^2/\nu$ for viscous-gravitational

drainage. Justification of the neglect of the inertial terms demands that the Galilei number $Ga = Go^3\Gamma^{3/2}$ is small, which is satisfied for all tested fluids except for water ($\Gamma = 3376$). Our computations of the solutions to the CM equation (5) confirm these scaling arguments as shown in table II.

In Fig. 6, we contrast the wave profiles rescaled with respect to \bar{R} corresponding to Table II. Except from the front and back of the waves corresponding to the return to the fixed point, the wave profiles are rather symmetric. This front-to-back symmetry shows that gravity does not affect the wave profile, as expected, since the typical size of the wave \bar{R} is much smaller than the capillary length l_c . Therefore, solitary waves in this regime resemble isolated drops sliding under the action of gravity on a wettable fibre, which is precisely why we refer to this regime as the drop-like regime. [When \bar{R} is larger and approaches l_c , on the other hand, the drops will feel the effect of gravity as they grow and they will eventually resemble falling pendant drops.] It corresponds to the observation by Quéré [1, 25] in the coating of wires or thin fibres drawn out of a bath of viscous liquids that the thin annular film deposited on the wires/fibres breaks up into drops.

We have checked this analogy by computing the shape of static drops with zero contact angles sitting on a fibre coated with a substrate film of the same liquid (details of the calculation are given in Appendix B). The agreement of the wave shapes to the symmetrical static-drop shapes is remarkable even in the case of nearly spherical drops such as those obtained at $Go = 0.044$, where the long-wave assumption is no longer valid. We can therefore conclude that the CM equation (5), and by extension the WRIBL model (3), are accurate in the drop-like regime where surface tension is dominant and even if the long-wave approximation does not hold. Besides, the remarkable agreement between the solutions to the CM equation (5) and the WRIBL model (3) already noted in Fig. 2, shows that the second-order streamwise viscous terms do not affect the amplitude and speed of the drops.

Following [13], an analytical estimate of the amplitude and speed of the drop-like waves in the limit $Go \rightarrow 0$ may be obtained via matched asymptotic expansions. The appropriate small parameter is the dimensionless speed of the drops. By balancing viscous and capillary forces at the back of the waves, one can easily extend to sliding drops the Landau-Levich-Dejaguin law obtained by Quéré [25] in the case of fibres drawn out of a bath. The speed of sliding drops is thus governed by Eq. (B4) which compares favorably to the results from the CM equation in table II. As a matter of fact, this agreement shows that the thickness of the

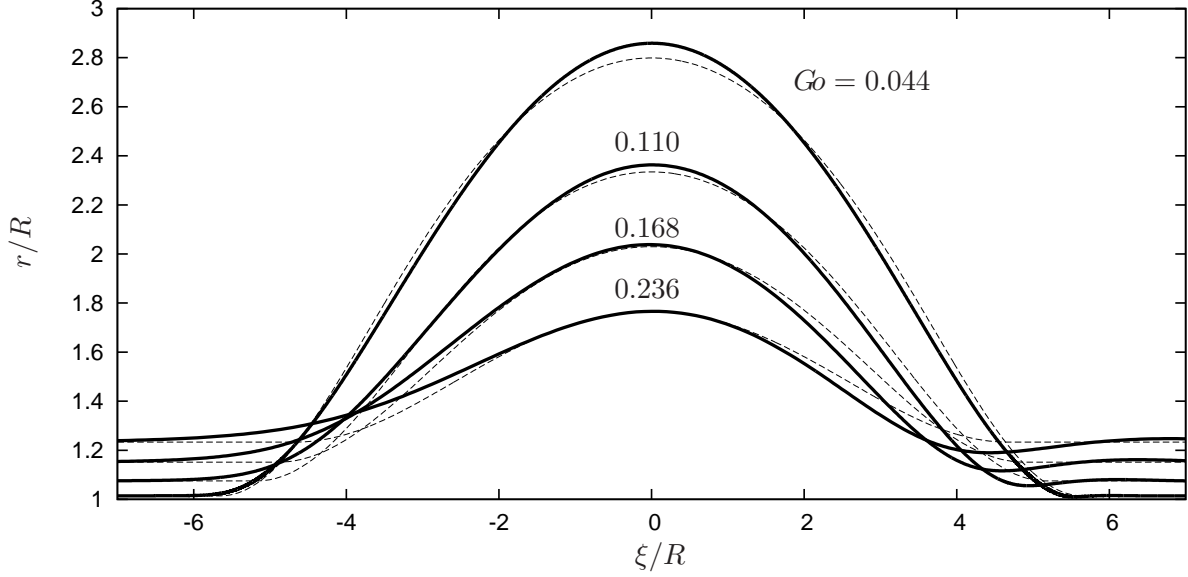


FIG. 6. Wave profiles corresponding to the solutions to the CM equation (solid lines) and static drop shape (thin dashed lines). Labels correspond to the Goucher number. Values of the other parameters are listed in table II.

residual film on which the drops slide is determined by the balance of surface tension and viscous dissipation in the meniscus region. To estimate the speed and amplitude of drop-like waves, one would have to take into account the gravity acceleration and higher-order corrections in the outer region, namely the viscous dissipation in the drop. A task which is difficult, as (a) with the Frenkel equation resolving fully the leading-order outer region requires matching up to third order [13] and quite likely this is the case here, (b) a single ‘composite equation’ for the whole domain, i.e. for both the drop and residuals films, as e.g. in the ‘drag-out’ problem in coating theory [32], does not exist.

B. Large δ limit: the drag-inertia regime

To understand the change of behaviour of the solitary-wave characteristics for $\delta \gg 1$, we look at the wave profiles and their projections on the plane (h, h') . Figure 7 compares two single-loop homoclinic orbits for a small and a large value of δ . For $\delta \ll 1$, solitary waves have a relatively symmetric shape. Except from the neighbourhood of the fixed point \mathbf{U}_I , where the escape from \mathbf{U}_I is monotonic and the return to it is oscillatory, a symmetry

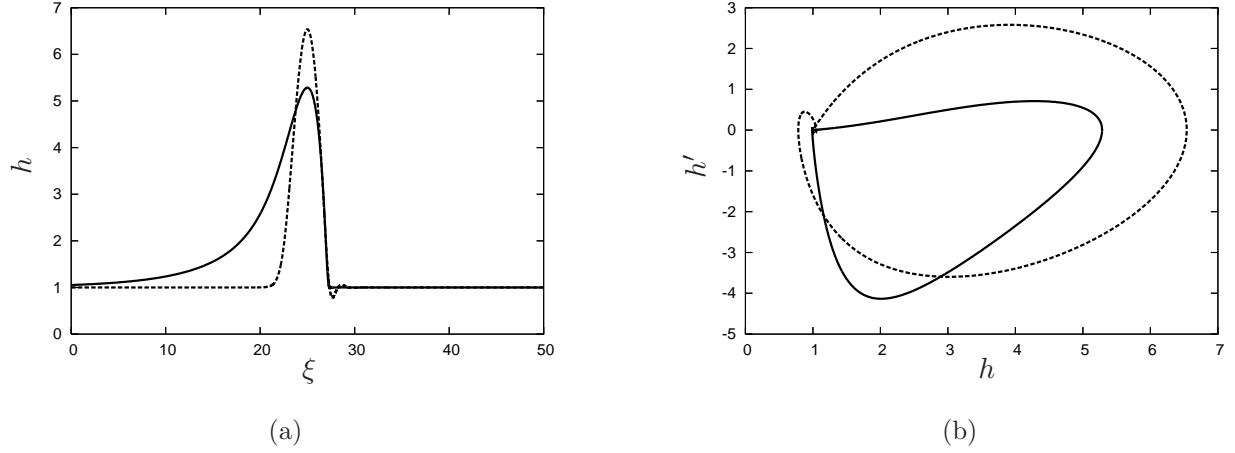


FIG. 7. Profile (a) and projected trajectory (b) onto the plane (h, h') of single-loop homoclinic solutions to (3) corresponding to single-hump solitary waves. Parameters correspond to Rhodorsil silicon oil v50 ($\Gamma = 5.48$) and $R = 0.25$ mm. Solid and dashed lines refer to $\delta = 5$ and $\delta = 3 \cdot 10^{-5}$, respectively.

between the front and back of the waves is observed with a steep front and a steep back. On the contrary, at large values of δ , the front and back of the solitary waves present radically different shapes, with a gentle sloping back edge and a steep front edge.

The observed difference between front and back of the solitary waves in the large- δ case can be explained by examining the linearised dynamics around \mathbf{U}_I . The dispersion relation governing infinitesimal perturbations varying as $\exp(\lambda\xi)$ is given in (16). At a given radius R and capillary length l_c , large thickness, $h_N \gg 1$, corresponds to $\delta \sim h_N^{11/3} \phi(\tilde{\alpha}) \gg 1$, $\beta/\delta = (l_c/R)^2/(3Re) \ll 1$ and possibly large viscous dispersion since $\eta \sim h_N^{4/3}$. Let λ_1 be the positive eigenvalue corresponding to the unstable manifold of \mathbf{U}_I . The eigenvalues of the tangent subspace to the unstable manifold satisfy $\text{Re}(\lambda_3) \leq \text{Re}(\lambda_2) < 0$. When \mathbf{U}_I is a saddle-focus ($\Delta > 0$), we further denote $\lambda_{2,3}$ by $-\Sigma \pm i\Omega$ with $\Sigma > 0$ and $\Omega > 0$. From (16) we obtain the estimate $\lambda_1 \sim \delta^{-1} \ll 1$. Since $\lambda_1 + \lambda_2 + \lambda_3 = -\eta D_\eta$, we immediately get an estimate of the mean value, $(\lambda_2 + \lambda_3)/2 \sim -\eta$, so that $\Sigma \sim \eta$ when $\Delta > 0$. As a consequence, at the back of a solitary wave, the monotonic escape from the fixed point is slow, whereas at the front, the return to \mathbf{U}_I is fast. The above estimates have been confirmed by computations of λ_1 and Σ for the solitary waves shown in Fig. 2 corresponding to silicon oil v50.

Focusing now at the back of the solitary wave and defining a slow variable $\tilde{\xi} = \xi/\delta$, (12)

reads,

$$\begin{aligned} & \left\{ (1 + \tilde{\alpha}h) \left[c^2 - cF(\tilde{\alpha}h) \frac{q}{h} \right] + G(\tilde{\alpha}h) \frac{q^2}{h^2} + \frac{\beta I(\tilde{\alpha}h)}{\delta(1 + \tilde{\alpha}h)^2 \phi(\tilde{\alpha})} \right\} \frac{dh}{d\tilde{\xi}} \\ &= \frac{I(\tilde{\alpha}h)}{\phi(\tilde{\alpha})} \left[\frac{3\phi(\tilde{\alpha})}{\phi(\tilde{\alpha}h)} \frac{q}{h^2} - h \right] + O(\eta/\delta^2, \delta^{-3}), \end{aligned} \quad (19)$$

where q is given by (11) and (15). Equation (19) can be formally rewritten as,

$$\mathcal{G}(h, c; \tilde{\alpha}, \beta/\delta) \frac{dh}{d\tilde{\xi}} = -\mathcal{H}(h, c; \tilde{\alpha}) + O(\eta/\delta^2, \delta^{-3}), \quad (20)$$

expressing the balance at the back of the solitary waves of inertia (at the left-hand side), viscous drag and gravity acceleration (at the right-hand side). As a consequence, the roots of the right-hand side of (19) correspond to the fixed points of (13).

As the homoclinic orbit departs from \mathbf{U}_I , h increases up to h_{II} which is larger than unity since $c > c_k$ (cf. Fig. 1). At this point, h goes through a maximum if \mathcal{G} is nonzero. The resulting orbit is thus a heteroclinic one linking \mathbf{U}_I and \mathbf{U}_{II} which contradicts the fact that we are considering a single-loop homoclinic orbit [10]. As a consequence, \mathcal{G} must go to zero at $h = h_{II}$ which signals a ‘critical film thickness’ h_c at which inertial terms must go to zero. In the limit $\delta \rightarrow \infty$, we thus obtain the condition

$$h_{II}(c; \tilde{\alpha}) = h_c(c; \tilde{\alpha}, \beta/\delta) \quad (21)$$

which gives a unique solution c_{crit} and then h_{crit} as function of $\tilde{\alpha}$ and β/δ . As the limit speed c_{crit} is governed by the balance of inertia, wall friction and gravity acceleration, we may refer to this situation as the *drag-inertia* regime [9].

Having shown that \mathcal{G} possesses at least one root, \mathcal{G} can be factorised into $\mathcal{G} = (1 + \tilde{\alpha}h)[c - c_{d+}(\tilde{\alpha}h, q/h, \beta/\delta)][c - c_{d-}(\tilde{\alpha}h, q/h, \beta/\delta)]$ where,

$$c_{d\pm}(\tilde{\alpha}h, q/h) = \frac{q}{h} \frac{F(\tilde{\alpha}h)}{2} \pm \sqrt{\Delta_{\tilde{\alpha}h, q/h, \beta/\delta}} \quad (22a)$$

$$\text{and } \Delta_{\tilde{\alpha}h, q/h, \beta/\delta} = \left(\frac{q}{h} \right)^2 \left[\frac{F(\tilde{\alpha}h)^2}{4} - \frac{G(\tilde{\alpha}h)}{1 + \tilde{\alpha}h} \right] - \frac{\beta I(\tilde{\alpha}h)}{\delta(1 + \tilde{\alpha}h)^3 \phi(\tilde{\alpha})}, \quad (22b)$$

are the speeds of linear dynamic waves for a uniform layer of thickness h and averaged speed q/h [17]. In other words, the position of the second fixed point must coincide with the critical layer h_c at which the speed of the solitary wave c is equal to the speed of one of the dynamic waves $c_{d\pm}$ – in fact the fastest one with speed c_{d+} –, which separates the flow into a ‘subcritical region’ ($c < c_{d+}$) and a ‘supercritical region’ ($c > c_{d+}$). The condition $h_{II} = h_{\text{crit}}$

is similar to the ‘Thomas condition’ derived in the mathematical treatment of periodic bores on steep slopes, or *roll-waves* [33, 34] made of the regular succession of laminar flows and hydraulic jumps. For $\delta \gg 1$, the front of the solitary waves, where surface tension arrests the breaking of the waves, plays a role similar to that of a hydraulic jump connecting the subcritical and supercritical regions of a roll wave. For this reason, we may also refer to this regime as the *roll-wave regime*.

Considering now large but finite values of δ , condition (21) is not verified and one has to go back to (20). At the critical point $h = h_c$ we have $\mathcal{G}(h_c, c; \tilde{\alpha}) = 0$ and a Taylor expansion close to criticality gives

$$h_c - h_{\text{crit}} \approx -[\partial_c \mathcal{G} / \partial_h \mathcal{G}](h_{\text{crit}}, c_{\text{crit}})(c - c_{\text{crit}}) \quad (23)$$

whenever $\partial_h \mathcal{G}(h_{\text{crit}}, c_{\text{crit}}) \neq 0$. Proceeding next to a Taylor expansion of $\mathcal{H}(h, c)$, (20) yields

$$\left[\partial_c \mathcal{H} - \frac{\partial_h \mathcal{H} \partial_c \mathcal{G}}{\partial_h \mathcal{G}} \right] (c - c_{\text{crit}}) \approx K_\eta \frac{\eta}{\delta^2} + \frac{K_{\text{st}}}{\delta^3}, \quad (24)$$

where the constants K_η and K_{st} are functions of h_{crit} , c_{crit} and the derivatives h'_{crit} , h''_{crit} and at h'''_{crit} at the critical thickness of the asymptotic solution. Since for $h_N \gg 1$, $\delta \sim h_N^{11/3}$ and $\eta \sim h_N^{4/3}$ the asymptotically dominant term in the right-hand-side of (24) are the viscous terms $K_\eta \eta \delta^{-2}$. Consequently, the convergence of the speed of the waves to the asymptotic value $c_{\text{crit}}(\tilde{\alpha})$ satisfies

$$c - c_{\text{crit}}(\tilde{\alpha}, \beta/\delta) \propto \eta/\delta^2 \sim 1/Re^2 \quad (25)$$

in agreement with our numerical computations.

Figure 8 compares the phase speed c of the solitary waves to the asymptotic limit c_{crit} as function of δ for the four different fluids of increasing viscosity that we considered (fluid properties are gathered in Table II). For weakly viscous flows, the RP and K mode reinforce each other and the speed c of the waves is much higher than the asymptote c_{crit} (see Fig. 8(a)). At larger viscosities (Figs. 8(b) and 8(c)) the K mode ceases to be affected by the RP instability and a rapid convergence to c_{crit} is observed as δ is increased. Whereas for very viscous fluids like silicon oil v1000 (one thousand times more viscous than water, cf. Table I), the curves start again to separate signalling the arrest of the convergence to the asymptote c_{crit} by the axial viscous effects.

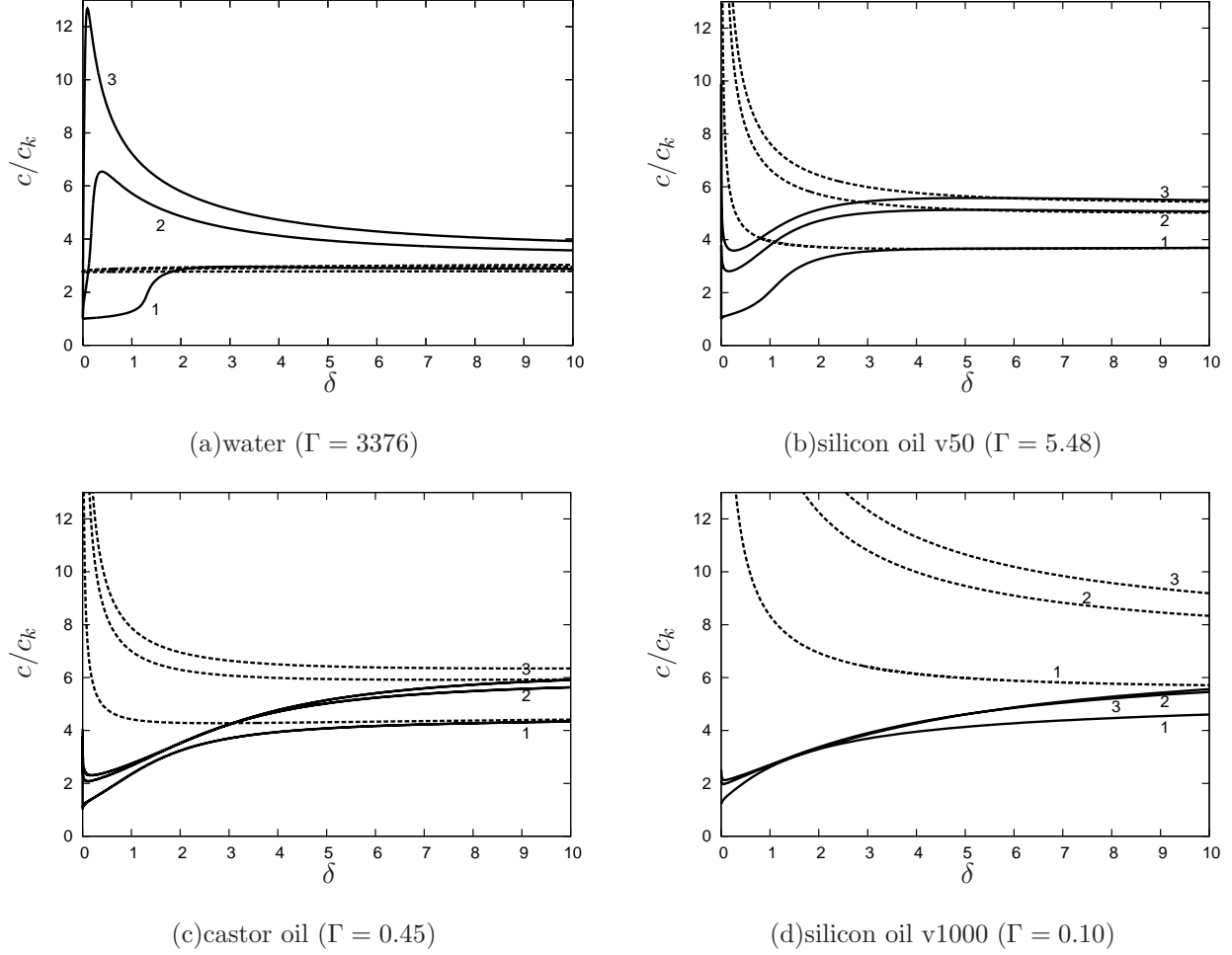


FIG. 8. Speed c of the solitary waves as function of the reduced Reynolds number δ for three values of the Goucher number $Go = 1.01$ (curves 1), 0.236 (curves 2) and 0.168 (curves 3) for fluids of decreasing Kapitza numbers. Solutions to (3) (solid lines) are compared to the asymptotic predictions c_{crit} (dashed lines).

C. Weakly nonlinear analysis

Let us now consider the regions of the speed and maximum height diagrams in Figs. 2, 4 and 5 corresponding to the transition between the drop-like regime and the drag-inertia regime. They correspond to situations where neither the K nor the RP instability mechanisms are strong enough to promote large amplitude waves, i.e. when $\delta \lesssim 1$ and $\beta^* \lesssim 1$. We can then proceed to a weakly nonlinear analysis to characterize the shape, speed and amplitude of the waves. Since $\delta \ll 1$, we substitute $h = 1 + H$ and $q = 1/3 + Q$ where

$H = O(\varepsilon)$ and $Q = O(\varepsilon)$ are small deviations from the base state $(h, q) = (1, 1/3)$, (i.e. $\varepsilon \ll 1$). Taking the distinguished limit $\varepsilon \ll \varepsilon^2$, we are led from the WRIBL (3) model to a single evolution equation for the deviation H :

$$\begin{aligned} \partial_t H + c_k \partial_x H + \Phi(\tilde{\alpha}) H \partial_x H + \frac{\beta}{3(1+\tilde{\alpha})^3} \partial_{xx} H + \frac{1}{3(1+\tilde{\alpha})} \partial_{xxx} H \\ + \delta \frac{\phi(\tilde{\alpha})}{3I(\tilde{\alpha})} \left[\partial_{tt} H + \frac{F(\tilde{\alpha})}{3} \partial_{tx} H + \frac{G(\tilde{\alpha})}{9(1+\tilde{\alpha})} \partial_{xx} H \right] \\ + \eta \frac{\phi(\tilde{\alpha})}{3I(\tilde{\alpha})} \left[M(\tilde{\alpha}) \partial_{xxt} H - \frac{L(\tilde{\alpha})}{3(1+\tilde{\alpha})} \partial_{xxx} H \right] = O(\varepsilon \varepsilon^5, \varepsilon^2 \varepsilon^2), \end{aligned} \quad (26)$$

where

$$\Phi(\tilde{\alpha}) = \frac{3(2+\tilde{\alpha})\phi + \tilde{\alpha}[(6+5\tilde{\alpha})\phi' + \tilde{\alpha}(1+\tilde{\alpha})\phi'']}{3(1+\tilde{\alpha})^2\phi} \quad (27)$$

is a function of the aspect ratio $\tilde{\alpha}$. Noteworthy is that a stability analysis of the base state $(h, q) = (1, 1/3)$ based on (26) leads to the same dispersion relation as for (3).

1. Drag-gravity regime

We consider here the limit of a thin film compared to the fibre radius, $\tilde{\alpha} \ll 1$, when the radius of the fibre is constant or equivalently Go is constant. Since $\eta = (\bar{h}_N/l_c)^{4/3} = \tilde{\alpha}^{4/3} Go^{4/3}$, viscous dispersion is negligible in this limit and (26) reduces to

$$\partial_t H + \partial_x H + 2H \partial_x H + \frac{\beta}{3} \partial_{xx} H + \frac{2}{5} \delta \left[\partial_{tt} H + \frac{17}{21} \partial_{tx} H + \frac{1}{7} \partial_{xx} H \right] + \frac{1}{3} \partial_{xxx} H = 0. \quad (28)$$

By making use of the first-order equivalence of the time- and space-derivatives of H , $\partial_t H \approx -\partial_x H$, (28) reduces to the Kuramoto-Sivashinsky (KS) equation:

$$\partial_t H + \partial_x H + 2H \partial_x H + \frac{1}{3} \left[\frac{2}{5} \delta + \beta \right] \partial_{xx} H + \frac{1}{3} \partial_{xxx} H = 0. \quad (29)$$

To look for the TW solutions to (29) in their moving frame, $\xi = x - ct$, we rescale the velocity as $c = 1 + C$, and the amplitude as $H = \varepsilon A$ and stretch the moving coordinate as $\xi = BX$:

$$-3CB^3 A + 3\varepsilon B^3 A^2 + B^2 \Upsilon \frac{d}{dX} A + \frac{d^3}{dX^3} A = 0, \quad (30)$$

where $\Upsilon = \frac{2}{5}\delta + \beta$ and the condition $\lim_{\xi \rightarrow \pm\infty} H = 0$ has been enforced yielding a vanishing integration constant. Balancing each term in (30) gives $CB^3 \sim \varepsilon B^3 \sim B^2 \Upsilon \sim 1$ so that $B \sim \Upsilon^{-1/2}$, $\varepsilon \sim \Upsilon^{3/2}$ and $C \sim \Upsilon^{3/2}$.

Writing $B = \Upsilon^{-1/2}$, $\varepsilon = \frac{2}{3}\Upsilon^{3/2}$ and $C = \mu\Upsilon^{3/2}/3$ then leads to

$$-\mu A + 2A^2 + \frac{d}{dX}A + \frac{d^3}{dX^3}A = 0, \quad (31)$$

which is an ordinary-differential equation governing the TW solutions to the KS equation propagating at speed μ . Equation (31) admits a one-hump solitary-wave solution for a particular value of $\mu = \mu_0 \approx 1.216$ and an amplitude $A_{\max} \approx 0.784$. Consequently, in the limit $\tilde{\alpha} \rightarrow 0$, the speed c and the amplitude h_{\max} of the one-hump solutions to (3) follow power laws of the form:

$$c \approx 1 + 0.405 \Upsilon^{3/2} \quad h_{\max} \approx 1 + 0.523 \Upsilon^{3/2}. \quad (32)$$

Recall that the relations (32) have been obtained under the assumption of small amplitude, $h_{\max} - 1 \ll 1$, hence Υ must be small, which implies that both inertia and azimuthal curvature effects must be small. Viscous drag and gravity acceleration are the dominant physical effects. Following [9], we may refer to this regime as the *drag-gravity regime*.

It is possible to interpret this regime as one characterized by the arrest of the instability growth by the flow advection. The dispersion relation corresponding to the KS equation (29) and governing infinitesimal perturbations around the base Nusselt flow of wavenumber k and angular frequency ω is identical to (7) when β is substituted with Υ . One can then follow the same line of reasoning in going from (7) to (8) and define the ratio of the typical time of advection of the structure over its length, $\tau_a = k^{-1}$, to the typical time of growth, $\tau_g = [\max(\omega_i)]^{-1}$, of the instability:

$$\tau_a/\tau_g = \omega_i/\omega_r|_{k=\sqrt{\Upsilon/2}} \propto \Upsilon^{3/2}. \quad (33)$$

Therefore $\Upsilon \ll 1$ corresponds to $\tau_a \ll \tau_g$. The flow advection is much faster than the instability and the ratio τ_a/τ_g controls the amplitude and speed of the observed structures as reflected by (32).

2. Soliton-like regime

We consider in this section the limit of a thick film, $\tilde{\alpha} \gg 1$, though in practice, if $\tilde{\alpha}$ is large, the axisymmetry of the flow might be difficult to achieve. We thus have $\phi(\tilde{\alpha}) \sim (3/4)\tilde{\alpha} \log(\tilde{\alpha})$, $c_k \sim 4/3\tilde{\alpha}^{-1}$ and $\beta^* \sim (3/4)^{2/3}(\tilde{\alpha}Go)^{-4/3}$, $\delta \sim \frac{3}{4}\tilde{\alpha} \log(\tilde{\alpha})\Gamma^{3/2}(\tilde{\alpha}Go)^{11/3}$ while

in all cases $\eta = (\tilde{\alpha}Go)^{4/3}$. Therefore the conditions $\delta \ll 1$ and $\beta^* \lesssim 1$, necessary to sustain the weakly nonlinear analysis, can be justified if e.g. $\tilde{\alpha}Go = O(1)$, i.e. $\eta = O(1)$ and $\Gamma^{3/2} \ll 1$. For silicon oil v1000, $\Gamma = 0.1$ so that $\Gamma^{3/2} = 0.03$. [We note that strictly speaking the derivation of the WRIBL model (3) demands that Γ is at least $O(1)$ since the long-wave approximation is sustained only when surface tension effects are strong [17].]

Neglecting inertial effects and looking for the dominant terms in (26) leads to

$$\begin{aligned} \partial_t H + \frac{4}{3\tilde{\alpha}} \partial_x H + \frac{8}{3\tilde{\alpha}} H \partial_x H + \frac{1}{3\tilde{\alpha}\eta} \partial_{xx} H + \frac{1}{3\tilde{\alpha}} \partial_{xxxx} H \\ - \eta \log(\tilde{\alpha}) \left[\frac{3}{2} \partial_{xxt} H + \frac{1}{\tilde{\alpha}} \partial_{xxx} H \right] = 0. \end{aligned} \quad (34)$$

The first-order equivalence of the time and space derivatives of H , i.e. $\partial_t H = -(4/(3\tilde{\alpha}))\partial_x H + O(\epsilon\varepsilon^2, \epsilon^2\varepsilon)$, can again be utilized. Equation (34) is then simplified into

$$\partial_t H + \frac{4}{3\tilde{\alpha}} \partial_x H + \frac{8}{3\tilde{\alpha}} H \partial_x H + \frac{1}{3\tilde{\alpha}\eta} \partial_{xx} H + \frac{\eta \log(\tilde{\alpha})}{\tilde{\alpha}} \partial_{xxx} H + \frac{1}{3\tilde{\alpha}} \partial_{xxxx} H = 0, \quad (35)$$

the ‘Kawahara’ equation that was scrutinized numerically by Kawahara and coworkers [35, 36]. The equation is also often referred to as the ‘generalized KS’ equation [20, 37, 38], and it is the KS equation appropriately extended to include dispersion ($\partial_{xxx} H$). As before, we look for TW solutions in their moving frame, $\xi = x - ct$. Stretching the moving coordinate as $\xi = \sqrt{\eta}X$, the amplitude as $H = \eta^{-3/2}A/2$, and the speed as $c = (4/3)\tilde{\alpha}^{-1}(1 + \mu\eta^{-3/2}/4)$, then gives

$$-\mu A + 2A^2 + \frac{d}{dX}A + \delta_K \frac{d^2}{dX^2}A + \frac{d^3}{dX^3}A = 0, \quad (36)$$

with $\delta_K = 3\eta^{3/2} \log(\tilde{\alpha})$ is a parameter that measures the relative importance of dispersion. Equation (36) governs TW solutions of the Kawahara equation propagating at speed μ . Since $\tilde{\alpha} \gg 1$ and $\eta = O(1)$, the dispersion parameter δ_K is large, in which case the speed of the one-hump solitary waves solutions to (36) is given by $\mu \approx 0.3256\delta_K$. Solitary wave solutions of (3) in the limit $\tilde{\alpha} \gg 1$ and $\delta \ll 1$ should therefore satisfy:

$$\frac{c}{c_k} \approx 1 + 0.24 \log(\tilde{\alpha}). \quad (37)$$

The speed of the one-hump solitary wave solutions to (3) is compared to the asymptotic limit (37) in Fig. 9(a). However, our computations show that for moderate values of $\tilde{\alpha}$ the wave speed is in fact closer to $c/c_k \approx 1.65 + 0.24 \log(\tilde{\alpha})$. The reason for this discrepancy can be traced in the violation of the assumption of small amplitude deviations from the base state ($h - 1 \ll 1$) that was necessary to obtain (35) from (3). Indeed, TW solutions to the Kawahara equation have a speed and an amplitude that diverge as δ_K becomes large.

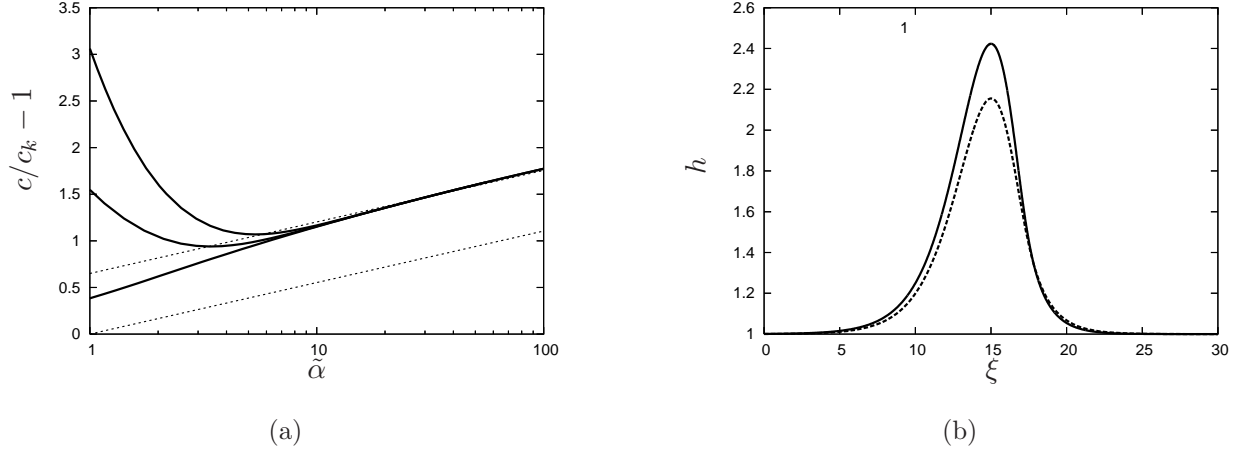


FIG. 9. (a) Speed of solitary wave solutions to (3) when inertia is neglected ($\delta \rightarrow 0$) as function of the aspect ratio $\tilde{\alpha}$. Dotted lines refer to (37) and to $c/c_k \approx 1.65 + 0.24 \log(\tilde{\alpha})$. (b) Profile of the solitary wave solutions to (3) with (solid line) and without (dashed line) inertial terms (castor oil $\Gamma = 0.45$, $R = 0.31$ mm, $\delta = 0.5$, $\eta = 0.45$ and $\tilde{\alpha} = 4.06$).

D. Speed to amplitude relation

The weakly nonlinear analysis presented in subsection IV C provides us with the dependencies (32) of the speed and maximum height as functions of $\Upsilon = \frac{2}{5}\delta + \beta$ for small film thicknesses. Combining these two relations give a linear dependence of the deviation amplitude $h_{\max} - 1$ to the deviation speed $c/c_k - 1$, where the wave speed c has been normalised with the kinematic wave speed c_k :

$$h_{\max} - 1 \approx 1.29 \left(\frac{c}{c_k} - 1 \right) \quad (38)$$

A linear dependence of the speed as a function of amplitude was initially found by Chang [39]

$$h_{\max} - 1 \approx \frac{c}{c_k} - 1 \quad (39)$$

by utilizing a normal form analysis of the TW solutions of the KS equation (29). This linear dependence is a characteristic of the drag-gravity regime and must be contrasted with the experimental relation

$$h_{\max} - 1 \approx 1.67 \left(\frac{c}{c_k} - 1 \right) \quad (40)$$

obtained by Tihon *et al.* [40] for solitary waves running down a plane inclined at an angle 5° . A linear dependence of h_{\max} with respect to c/c_k has also been found experimentally in the recent study by [5] for solitary waves on a relatively thick fibre.

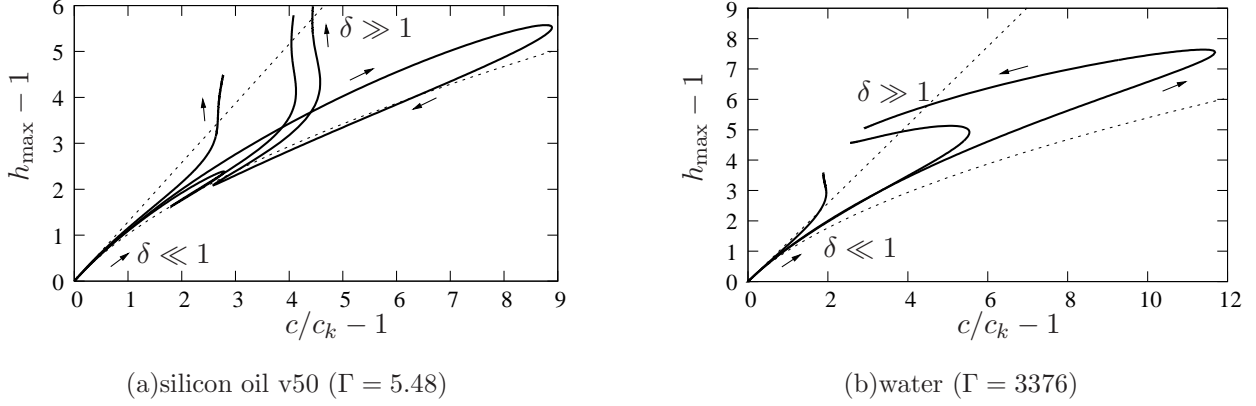


FIG. 10. Deviation wave amplitude $h_{\max} - 1$ versus relative wave speed $c/c_k - 1$ for the solitary-wave solutions to (3) for $Go = 1.01, 0.236$ and 0.168 . The dashed lines correspond to the estimates (38) and (41).

Similarly, in the drop-like regime, a law relating c and h_{\max} can easily be obtained by recognizing that the wave amplitude $h_{\max} - 1$ should be proportional to the distance $h_{\text{II}} - 1$ separating the fixed points. The constant of proportionality is determined by continuity with (38) in the limit $h_{\text{II}} - 1 \ll 1$ for which $h_{\text{II}} - 1 \approx c/c_k - 1$ (see Fig. 1). Next, by approximating h_{II} with $-1/2 + \sqrt{3[c/c_k - 1/4]}$ we arrive at:

$$h_{\max} - 1 \approx 1.29 \left(-\frac{3}{2} + \sqrt{3 \left[\frac{c}{c_k} - \frac{1}{4} \right]} \right). \quad (41)$$

Figure 10(a) presents the dependency of $h_{\max} - 1$ on the relative speed $c/c_k - 1$ for the results in figure 2 corresponding to the WRIBL model (3) and to silicon oil v50. The direction of increasing reduced Reynolds number δ along the curves is indicated by arrows. There is good agreement with relation (38) in the limit $c \approx c_k$. A good agreement with relation (41) is also found in the case of the fast waves ($c/c_k > 6$), typical of the drop-like regime observed at small Goucher numbers. In the drag-inertia regime, however, at large values of δ , the speed of the waves saturates to the limit $c_{\text{crit}}(\tilde{\alpha}, \beta/\delta)$ and no univocal mapping of the amplitude to the wave speed is observed.

When the drop-like regime is affected by inertia for weakly viscous liquids, the linear relation (41) is no longer applicable reflecting the influence of the K mode on the drop-like waves and in particular the steepening of the wave fronts (see Fig. 10(b)).

It is then clear from the above, that equation (41) provides a good approximation to the

speed-to-amplitude dependence for solitary waves both in the drop-like and the drag-gravity regime.

V. TRAVELING WAVES

In this section, we compare periodic TW solutions of the WRIBL model (3) —i.e. limit cycles of the dynamical system (13)— with ($\eta \neq 0$) and without viscous dispersion ($\eta \rightarrow 0$) and of the CM equation (5) (both $\delta \rightarrow 0$ and $\eta \rightarrow 0$), for the experimental conditions considered by [2] and [4]. We revisit the description of the TWs branches of solutions given in [17] with reference to the characteristics of TWs of infinite extension, i.e. as TWs approach homoclinicity. In the experimental set-ups of [2, 4] the flow rate was controlled and maintained at a constant value at the inlet. Amplification of the ambient noise resulted in a wavy dynamics with waves traveling with constant shapes and speeds over long distances. Periodic TWs can be produced experimentally by applying periodic perturbations at the inlet [5, 41]. If the signal remains periodic in time at each location in space, an integration in time of the mass balance (3a) shows that the time average of the flow rate, $T^{-1} \int_0^T q dt$, where T is the period, is conserved all along the fibre and is equal to its value at the inlet which gives the condition $T^{-1} \int_0^T q dt = 1/3$ [42]. Periodic TW solutions of the model equations aiming to describe the experimental conditions must therefore verify the condition $\langle q \rangle \equiv k/(2\pi) \int_0^{2\pi/k} q d\xi = 1/3$, where k again denotes the wavenumber.

Let us first consider the experimental conditions corresponding to the very viscous fluid considered by [2] (castor oil, $\Gamma = 0.45$; see Table I). The bifurcation diagram of TW solutions of the WRIBL model (3) and of the CM equation (5) are compared in Figure 11(a). The parameters in the figure correspond to regime ‘c’ reported by Kliakhandler *et al.* ($q_N = 21$ mg/s and $R = 0.25$ mm). We have normalised the wavenumber k with the reference $k_{RP} \equiv \sqrt{\beta}/(1 + \tilde{\alpha})$ corresponding to the marginal stability condition (real k and ω) for linear waves solutions to the CM equation k_{RP} corresponds to a dimensional wavelength $2\pi(\bar{R} + \bar{h}_N)$ proportional to the diameter of the liquid cylinder.

Figure 11(c) shows corresponding wave profiles with regularly spaced streamlines in the moving frame, i.e. iso-contours of the function $\psi = \int_R^r u_x r dr + c(R^2 - r^2)/2$ at levels nq_0/N , $1 \leq n \leq N$ with $N = 10$. The surface of the fibre corresponds to $\psi = 0$ and the free surface to $\psi = q_0$. In the case of the WRIBL model (3), only one branch of TW solutions

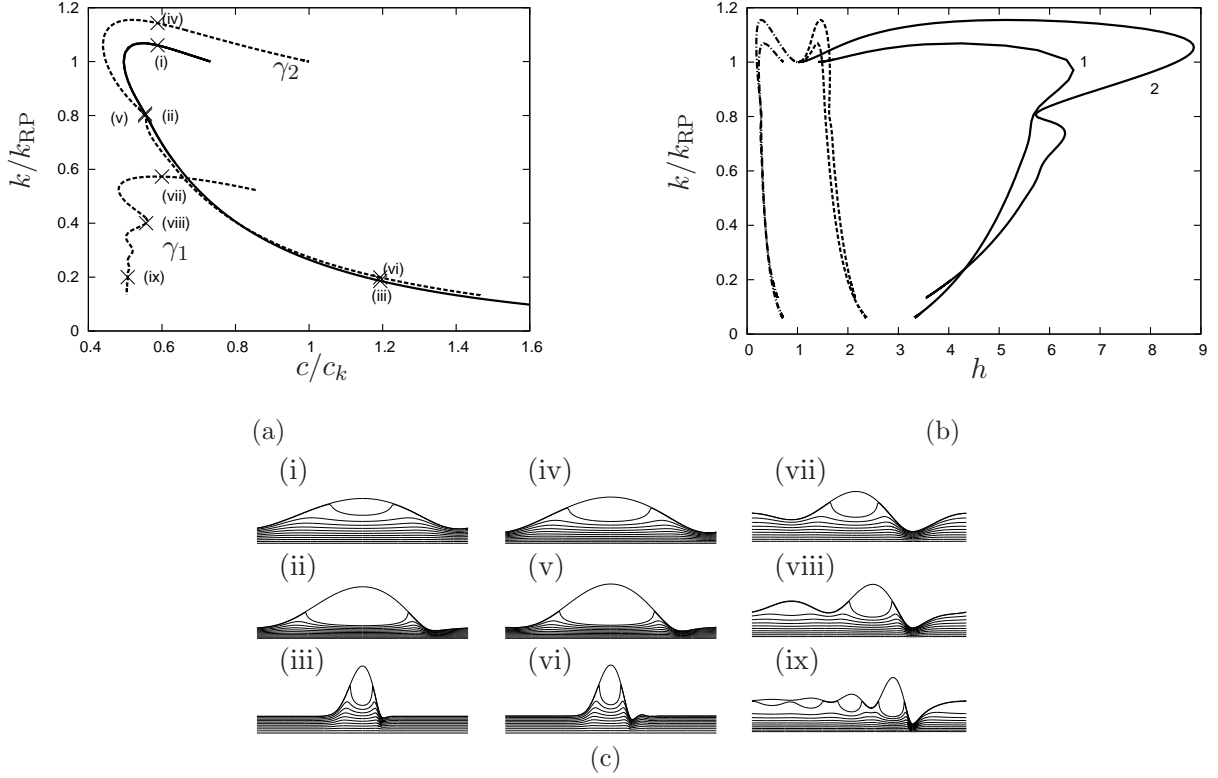


FIG. 11. TW branch of solutions bifurcating from the marginal stability conditions. (a) Normalised speed c/c_k as function of the normalised wavenumber k/k_{RP} where $k_{RP} = \sqrt{\beta}/(1 + \tilde{\alpha})$ (see text). Solid and dashed lines refer to (3) and to the CM equation (5), respectively. (b) Maximum thickness h_{max} (dashed line) and substrate thickness h_s (dashed-dotted line) as functions of the normalised wavenumber k/k_{RP} . The solid line refers to the relative maximum thickness h_{max}/h_s . Labels 1 refer to model (3), whereas labels 2 refer to the CM equation (5). (c) Wave profiles and streamlines in the moving frame for solutions indicated by crosses in panel a; left: solutions to (3); right: solutions to (5). Parameters correspond to the experimental conditions of [2]: $q_N = 5.3$ mg/s and $R = 0.25$ mm ($Go = 0.138$, $\tilde{\alpha} = 2.04$, $\delta = 0.01$, $\eta = 0.18$ and $\beta^* = 2.1$).

has been found emerging from the marginal linear stability conditions at $k \approx k_{RP}$ through a Hopf bifurcation, whereas a secondary branch has also been found by period doubling for the CM equation (5). We note that weakly nonlinear TW solutions of (3) travel at a smaller speed than the TW solutions of the CM equation (5) since the speed of linear kinematic waves is significantly affected by the second-order viscous effects [17]. At small wavenumbers, TW solutions of the branch emerging from $k \approx k_{RP}$ accelerate, become more

and more localized and terminate into the single-hump solitary waves discussed in § III. The speed, amplitude and shape of the solutions of (3) and (5) are comparable in this limit. Following the terminology introduced by Chang and co-workers for falling films on a planar substrate [43, 44], we refer to this branch of solutions as the ‘ γ_2 waves’. The branch of solutions to (5) emerging through period doubling terminates by slow waves with a shape made of a trough followed by capillary ripples. Following again [43, 44] for planar substrates, we refer to these TWs as the ‘ γ_1 waves’.

For the conditions of Fig. 11, the fibre radius is small compared to the capillary length ($Go = 0.138$) and the Nusselt film thickness is comparable to the fibre radius ($\tilde{\alpha} = 2.04$). As a consequence, the RP instability mechanism is strong and TWs have amplitudes comparable to the fibre radius, which corresponds to the typical situation of the ‘drop-like’ regime of the solitary waves discussed in § IV A. Yet, a direct transposition of the results obtained in § IV A to solitary-like wavetrains in the limit $k \rightarrow 0$ is not possible since the reference thickness of the substrates of the solitary-like waves is not constant (recall that in the treatment of solitary wave solutions, the constant film thickness far from the solitary waves was the reference thickness). We have computed the parameter β_s^* based on the substrate thickness h_s defined by the position of the fixed point in the phase space when the corresponding limit cycle approaches homoclinicity. The maximum of the relative thickness h_{\max}/h_s , 6.5 here, is reached for a value of the local number β_s^* close to its maximum, namely 3.65, as expected since the waves’ characteristics are piloted by the balance between the advection by the flow and the RP instability in the drop-like regime. Figure 11(b) shows the evolution of the maximum thickness, h_{\max} , of the substrate thickness h_s and of the ratio of the two as function of the normalised wavenumber k/k_{RP} . At small k , a TW is solitary-like and travels on a portion of nearly flat substrate of increasing length. The mass transported by the wave decreases in comparison to the mass carried by the substrate and h_s asymptotes to the Nusselt film thickness. As a consequence h_s increases as k tends to zero. This trend is followed by the maximum height h_{\max} . As a TW gets more and more localized, it tends to have bigger and bigger size. However, the maximum relative thickness, h_{\max}/h_s , is a rapidly decreasing function of k at small wavenumbers. Indeed, larger substrate thicknesses imply weaker RP instability mechanisms and stronger advection: β_s^* (not shown) follows a trend similar to h_{\max}/h_s . We therefore obtain a rather paradoxical picture: Despite the weakening of the RP instability — thus the lowering of h_{\max}/h_s —, a TW has its absolute amplitude

augmented as k tends to zero.

For the experiments by Kliakhandler *et al.*, the RP instability mechanism is strong while inertia and viscous dispersion are weak ($\delta = 0.01$, $\eta = 0.18$) which explains the good agreement obtained with the results from the CM equation (5). However, as the RP instability is weakened by raising the Goucher number, streamwise viscous dispersion should play an increasingly important role. We have checked this by computing the TW solutions of (3) and (5) corresponding to a flow rate $q_N = 10$ mg/s and a larger radius $R = 0.5$ mm, i.e. for $\delta = 0.01$, $\beta^* = 1.16$ and $\eta = 0.22$, parameters that are comparable to those corresponding to the regime ‘c’ discussed by Kliakhandler *et al.* ($\delta = 0.01$, $\beta^* = 2, 1$ and $\eta = 0.18$) but with a value of $\beta^* \sim$ two times smaller. Branches of solutions are compared in figure 12(a) in the $(k/k_{RP}, c/c_k)$ -plane. γ_2 fast TW solutions of (5) are again observed to emerge from the marginal conditions $k \approx k_{RP}$ whereas γ_1 solutions are obtained through a period doubling bifurcation of the γ_2 branch. We note again that only the γ_2 branch of solutions can be found for the WRIBL model (3), with no period doubling bifurcation being detected in this case. We therefore conclude that the inclusion of second-order viscous effects reduces the number of wave families and, as a consequence, it may drastically simplify the complex sequence of bifurcations and topological structure of associated bifurcation diagrams. In fact, such a reduction of the number of wave families by the second-order viscous terms was also evidenced in the planar case [45].

In comparison to Fig. 11(a), the γ_2 branches portrayed in figure 11(a) now deviate significantly from each other even at small wavenumbers. The TW solutions of model (3) have a larger amplitude than the TW solutions of equation (5) as indicated in Fig. 12 which compares the wave profiles of waves of equal wavenumber. When approaching homoclinicity, this effect is enhanced, and solutions of (3) travel with a notably higher speed and larger amplitude than solutions of (5). They are also preceded by smaller capillary ripples.

Figure 12(b) compares h_s and h_{\max} . Again, the substrate thickness and the maximum thickness have the same trend as k tend to zero whereas the maximum relative thickness h_{\max}/h_s evolves in the opposite direction. However, a comparison of Fig. 12(b) to Fig. 11(b) reveals that the maximum reached by h_{\max}/h_s is \sim three times smaller than with the experimental conditions considered by [2]. Computations of the local values of the parameters based on the substrate thickness show that β_s^* does not exceed 1.41 and decreases with k whereas η_s increases. The local parameters are $\beta_s^* = 1.2$ and $\eta_s = 0.19$ for the wave profile

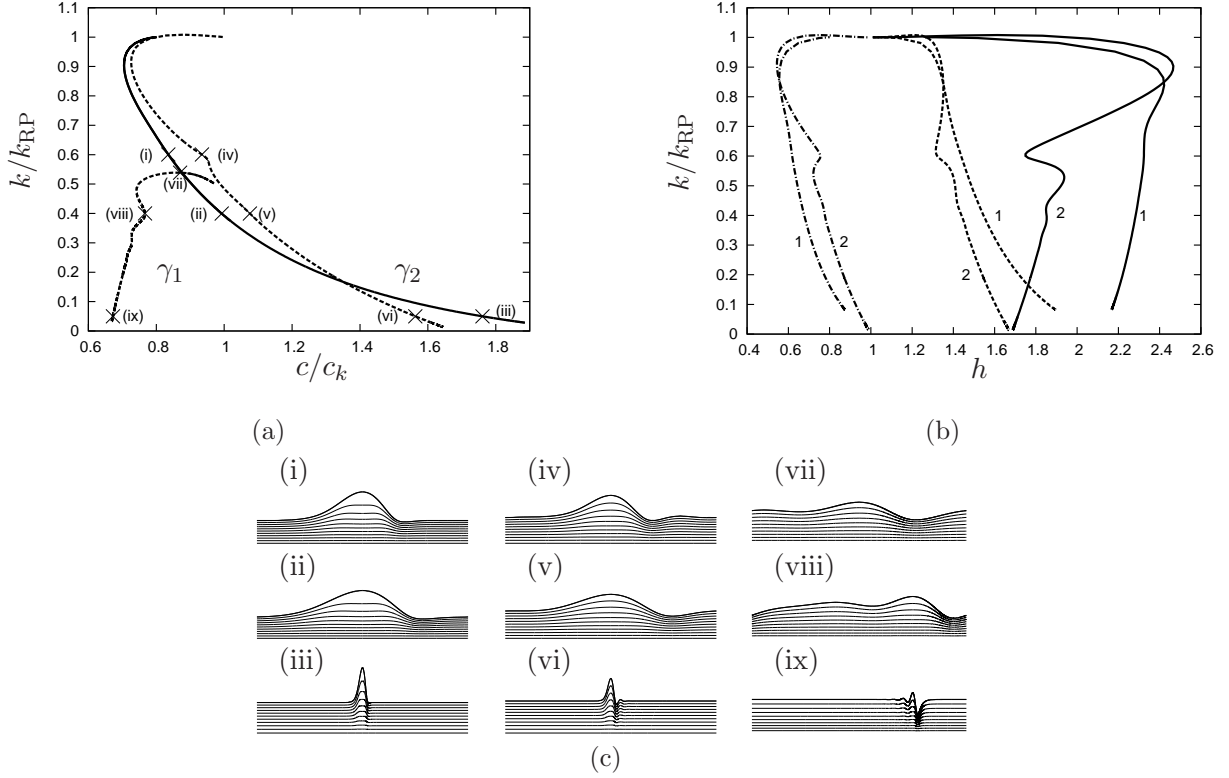


FIG. 12. TW branch of solutions bifurcating from the marginal stability conditions. Parameters correspond to castor oil ($\Gamma = 0.45$), $q_N = 10$ mg/s and $R = 0.5$ mm ($\delta = 0.01$, $\eta = 0.22$, $\tilde{\alpha} = 1.15$ and $\beta^* = 1.16$). See caption of figure 11.

labelled (iii) in Fig. 12 so that viscous dispersion effects start to be comparable with the RP instability mechanism. We conclude that viscous dispersion has a non-trivial amplifying effect on the RP instability mode.

For less viscous fluids like Rhodorsil silicon oil v50, one may expect a more significant effect of inertia and of the K mode of instability. In Fig. 13(a), we compare the substrate, maximum and relative maximum thicknesses, h_s , h_{\max} and h_{\max}/h_s , respectively, corresponding to the TW branch of solutions to (3). Parameters are chosen to correspond to one of the experimental conditions considered by [4] ($R = 0.23$ mm, $q_N = 151$ mg/s) and to a Goucher number $Go = 0.155$ close to the corresponding one for the experiments in [2] ($Go = 0.137$).

As k is lowered and the TWs approach homoclinicity, h_s and h_{\max} grow, a trend similar to what is observed in figures 11(b) and 12(b) for a more viscous fluid. However, the relative amplitude h_{\max}/h_s follows a surprising non-monotonic behaviour with an S-shape curve in

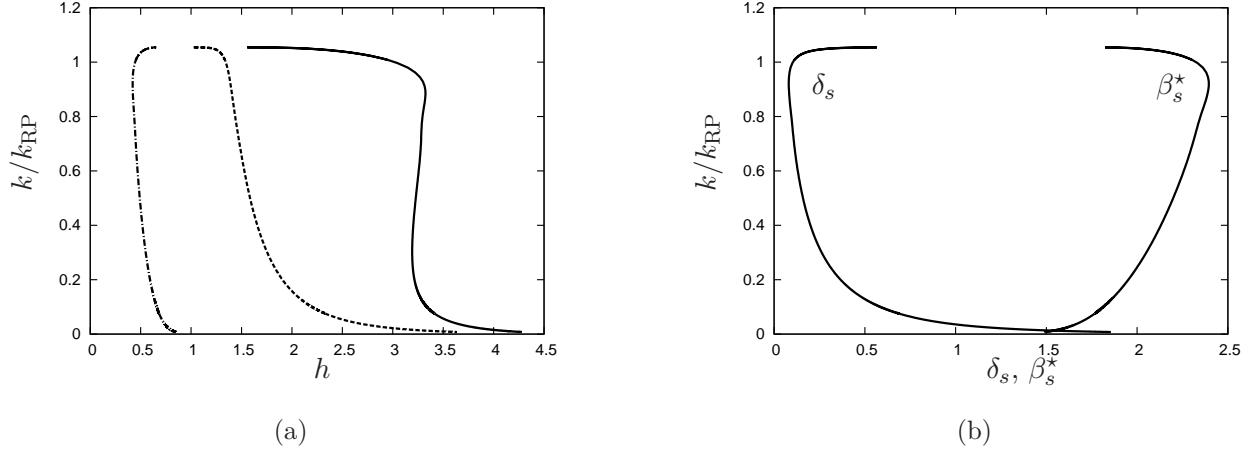


FIG. 13. (a) Maximum thickness h_{\max} (dashed line) and substrate thickness h_s (dashed-dotted line) versus the normalised wavenumber k/k_{RP} . The solid line refers to the relative thickness h_{\max}/h_s . (b) Local reduced Reynolds number δ_s and β_s^* versus k/k_{RP} . Parameters correspond to Rhodorsil v50 silicon oil ($\Gamma = 5.48$), $q_N = 151$ mg/s and $R = 0.23$ mm ($Go = 0.155$, $\delta = 3.9$, $\tilde{\alpha} = 3.0$ and $\eta = 0.36$).

the plane $(h, k/k_{\text{RP}})$. This behaviour can be understood by examining the local values of δ and β^* based on the substrate thickness h_s and presented in figure 13(b). As k is lowered to zero, β_s^* decreases whereas δ_s varies in the opposite direction. As a result, the two curves ultimately cross and very long waves correspond to a relatively stronger K instability mode than the initially dominant RP instability. We thus recover the usual trend observed with the solitary waves propagating on a planar film: Larger substrates imply larger amplitudes h_{\max} and also larger relative amplitude h_{\max}/h_s [44, 46].

We now turn to the experimental conditions considered in [5] corresponding again to Rhodorsil silicon oil v50 but with a larger fibre, $R = 0.475$ mm. The chosen flow rate $q_N = 296$ mg/s gives values of the reduced Reynolds number δ and of the viscous dispersion parameter η which do not vary significantly (compare e.g. $\delta = 4.1$ and $\eta = 0.44$ to $\delta = 3.9$ and $\eta = 0.36$). Inertia and viscous dispersion effects are therefore comparable whereas the RP instability mechanism is significantly lowered (β^* is reduced from 1.30 to 0.77). As for $R = 0.5$ mm and $q_N = 10$ mg/s, we found a single branch of TW solutions bifurcating from the marginal stability curve and the obtained bifurcation diagram (not shown) is similar to Fig. 12. Figure 14(a) compares the corresponding substrate thickness h_s , the absolute and

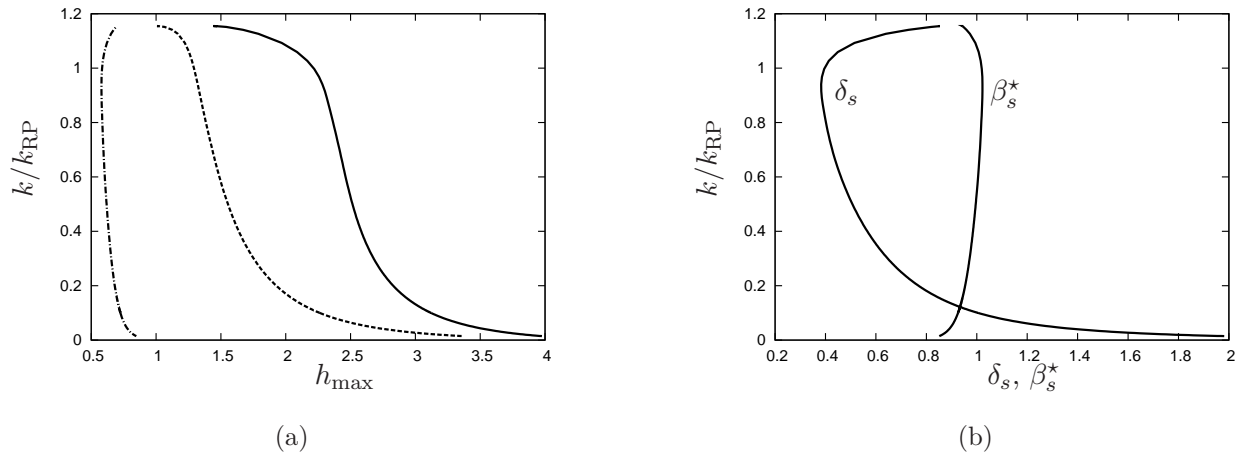


FIG. 14. (a) Maximum thickness h_{max} (dashed line) and substrate thickness h_s (dashed-dotted line) versus the normalised wavenumber k/k_{RP} . The solid line refers to the maximum relative thickness h_{max}/h_s . (b) Local reduced Reynolds number δ_s and β_s^* versus k/k_{RP} . Parameters correspond to Rhodorsil v50 silicon oil, $q_N = 296\text{mg/s}$ and $R = 0.475\text{ mm}$ ($Go = 0.32$, $\delta = 4.1$, $\tilde{\alpha} = 1.7$ and $\eta = 0.44$).

relative amplitudes h_{max} and h_{max}/h_s . As k is lowered, all curves exhibit a similar monotonic shape similar to what is expected in the planar case. Again, this can be understood by examining the local values of the two governing parameters (cf. Fig. 14(b)). The local reduced Reynolds number β_s^* does not exceed unity whereas δ_s sharply increases for very long waves, which signals the prevalence of the K mode over the RP mode.

Interestingly, TWs can be found at a wavenumber k higher than the critical wavenumber $k_c \approx k_{\text{RP}}$ corresponding to the marginal stability conditions, in which case the Nusselt solution is linearly stable. This subcritical bifurcation of TW solutions from the Nusselt uniform film occurs at small radii of the fibre, i.e. small Goucher number (see figures 11 and 12). The subcritical onset of TWs has also been reported in the recent work by Novbari and Oron [47] based on an ‘energy integral method’ though these authors did not give a physical interpretation of this phenomenon. Since the RP instability mechanism is strong when $Go \ll 1$, we can conjecture that the onset of subcriticality is related to surface tension effects associated with the azimuthal curvature (hence this effect is absent in the planar case). From a thermodynamic viewpoint, surface forces tend to reduce the free energy of the system and equilibrium is reached when the contact area between the liquid and the

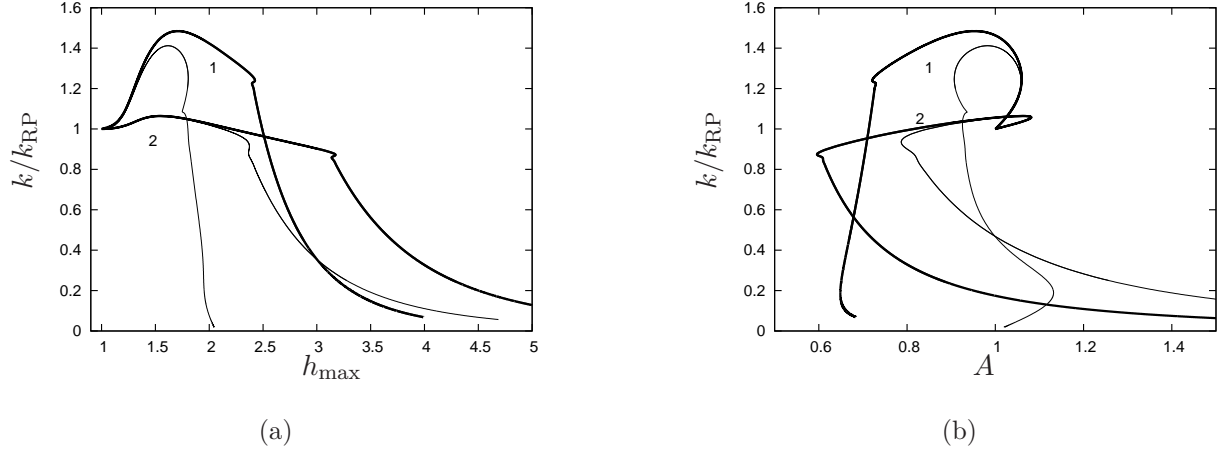


FIG. 15. Traveling wave solutions to the CM equation (5) for $\tilde{\alpha} = 8$ and $\tilde{\alpha} = 0.5$. Thick and thin solid lines refer to $Go = 0.02$ and $Go = 0.055$, respectively. Curves labeled 1 (respectively 2) correspond to $\tilde{\alpha} = 8$ ($\tilde{\alpha} = 0.5$).

surrounding gas is minimum. Obviously, the flow is out of equilibrium and a thermodynamic argument must be taken with care [48]. Yet, when $\delta \ll 1$, $\eta \ll 1$ and $Go \ll 1$, model (3) reduces at leading order to the long-wave Young-Laplace equation and the shape of the TWs thus only slightly differs from the shape of static drops on fibres as was shown in §IV A and in Fig. 6.

We have computed the TW solutions to the CM equation (5) for $Go = 0.02$ and $Go = 0.055$, and for $\tilde{\alpha} = 0.5$ and $\tilde{\alpha} = 8$. The maximum amplitude h_{\max} , and the interfacial area A of the waves normalised by the area of the uniform film solution of the same volume are displayed in Fig. 15. The subcritical onset of the TW solutions is accompanied by a normalized interfacial area lower than unity, and therefore a lowering of the free surface energy in comparison to the Nusselt uniform film solutions, which supports our conjecture that subcriticality is promoted by capillary effects. We note that the minimum wavenumber at which TWs are observed seem to depend only on $\tilde{\alpha}$ independently of Go . Conversely, at a given value of $\tilde{\alpha}$, the amplitude of the waves is strongly affected by the value of Go , a small Goucher number implying larger waves as expected, since the saturation number $\beta = \tilde{\alpha}^{2/3} Go^{-4/3}$ is also larger.

In Fig. 16 the maximum of the normalised wavenumber k/k_{RP} of the TW solutions of the CM equation is depicted as function of the aspect ratio $\tilde{\alpha}$ for $Go = 0.02$ and $Go = 0.055$. We note again that the location of this local maximum only weakly depends on the

Goucher number. The shape of the corresponding TW solutions (not shown) is also nearly symmetrical. We thus conclude that the subcritical behavior of the TW solutions is not affected by gravity effects at small values of the Goucher number but is strongly dependent on the parameter $\tilde{\alpha}$ and therefore on the geometry of the base flow.

By neglecting gravity effects and assuming a wettable substrate, the shape of a static drop is governed by its length and volume. Therefore, for a normalized area A set to unity, the shape of a static drop depends only on the aspect ratio $\tilde{\alpha}$ of the uniform film solution with the same volume. The solid line curve in figure 16 represents the wavenumber of static drops with unit normalized areas. Above this curve, $A > 1$ and the static drop solution is not energetically favorable, whereas below it the static drop solution is favored. Indeed, large drops have a nearly spherical shape with an interfacial area that is lower than the uniform film with the same volume, with further lowering of the interfacial area being forbidden by the presence of the fibre. For a given amount of liquid, the thicker the uniform film solution is, the lower the normalized area of the static drop would be. Therefore, the range of energetically favored wavenumbers of the static drop solution increases with the aspect ratio $\tilde{\alpha}$ as can be observed from figure 16.

We can now deduce two more arguments from Fig. 16 which support a capillary origin of the subcritical behavior of the branch of TW solutions that emerge from the Hopf bifurcation of the uniform film solution: (i) Since all points lie below the solid curve, TWs only exist when an energetically favorable static drop solution is available; (ii) The trend of the maximum of the TW wavenumber with respect to the aspect ratio $\tilde{\alpha}$ is similar to the trend of the boundary separating energetically favored and unfavored static drop solutions.

VI. PHASE DIAGRAM

We are now in a position to give a phase diagram of the different regimes found for all possible TW solutions on a film flow down a fibre. The onset of the ‘drop-like’ regime and the ‘drag-inertia’ regime corresponds roughly to $\beta^* \approx 1$ and $\delta \approx 1$. The ‘soliton-like’ regime arises when the instability mechanisms are weak ($\delta \lesssim 1$ and $\beta^* \lesssim 1$), the film is thick, $\tilde{\alpha} = O(1)$, and viscous dispersion is strong, $\eta = O(1)$. Finally, the ‘drag-gravity’ regime is observed when all other effects are weak ($\delta \lesssim 1$ and $\beta^* \lesssim 1$ and $\eta \ll 1$). Therefore, a phase diagram can be obtained for a given fluid, thus a given Kapitza number Γ , by

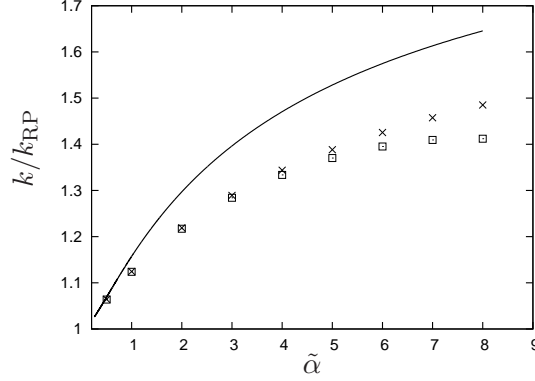


FIG. 16. Location of the maximum of the normalised wavenumber k/k_{RP} as function of the aspect ratio $\tilde{\alpha}$ for the TW solutions of the CM equation (5). Crosses (respectively squares) correspond to $Go = 0.02$ ($Go = 0.055$). The solid line denotes the static drop solution to (B1) with a normalized area $A = 1$ (see text and Appendix B).

drawing the curves $\delta = 1$, $\eta = 1$ and $\beta^* = 1$ in the plane $(\tilde{\alpha}, Go)$. Since $\eta = (\tilde{\alpha}Go)^{4/3}$ and $\beta^* = \{\tilde{\alpha}c_k(\tilde{\alpha})/[Go^2(1 + \tilde{\alpha}^4)]\}^{2/3}$ are functions of $\tilde{\alpha}$ and the Goucher number only, the corresponding curves $\beta^* = 1$ and $\eta = 1$ are independent of the working fluid considered. Thus, $\delta = 1$ is the only boundary that moves in the plane $(\tilde{\alpha}, Go)$ when Γ is varied. Figure 17 is a tentative representation of the phase diagrams for the four working fluids considered in this study, from weakly viscous fluids like water with a high Kapitza number, $\Gamma = 3376$, to highly viscous fluids like silicon oil v1000 corresponding to a small Kapitza number, $\Gamma = 0.10$. In the case of water, a large overlap region exists for the ‘drop-like’ and the ‘drag-inertia’ regime corresponding to a mutual reinforcement of the two K and RP instabilities. The ‘soliton-like’ regime takes over at relatively high viscosities where the curve $\delta = 1$ moves below the curve $\eta = 1$.

VII. CONCLUSIONS AND DISCUSSION

We have presented new results and insights on the characteristics of axisymmetric waves propagating down a fibre. Our analysis was based on the two-equation model derived in [17] using a weighted-residuals approach, equation (3). The model accounts for all physical effects, namely inertia, azimuthal curvature and viscous dispersion and has been validated in the studies by Ruyer-Quil *et al.* [17] and Duprat *et al.* [5] through direct comparisons to

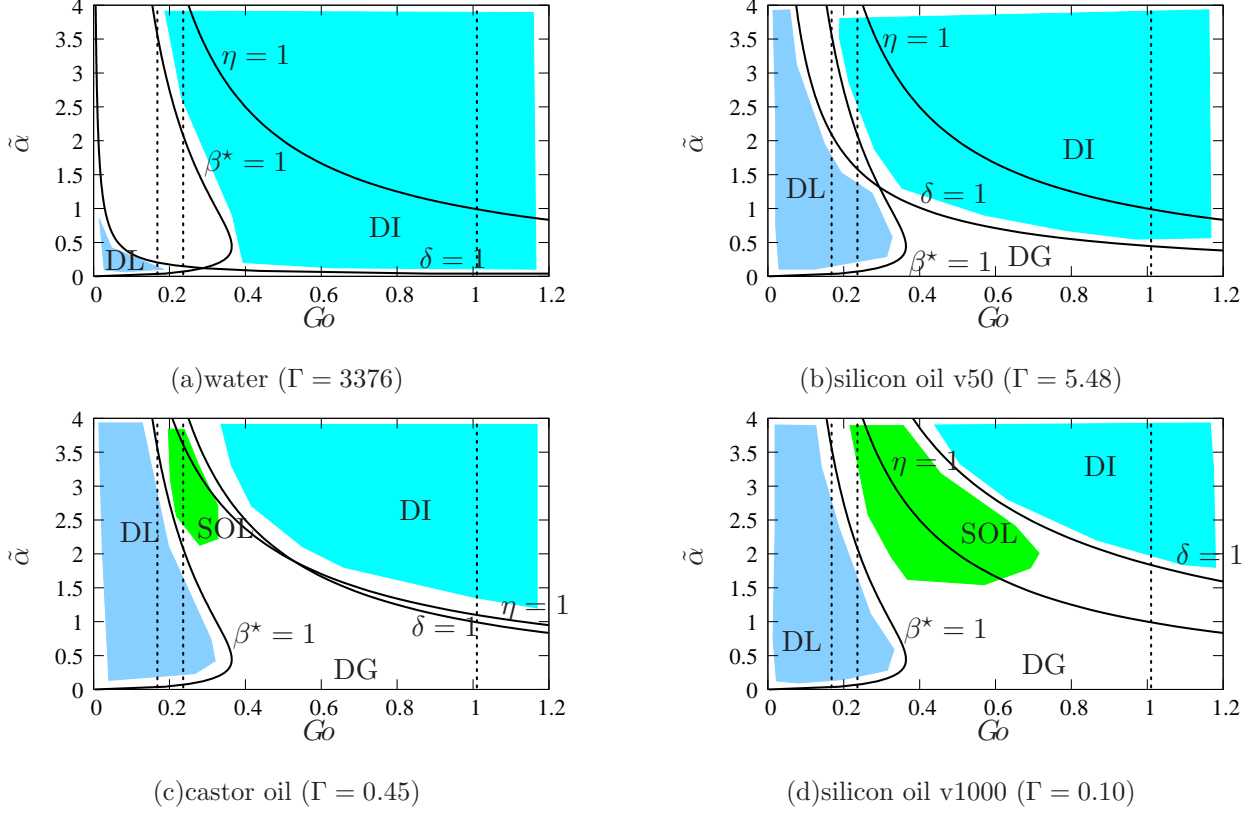


FIG. 17. Maps of the different regimes in the $Go - \tilde{\alpha}$ parameter space for fluids of increasing viscosity. The different curves are the loci of $\delta = 1$, $\eta = 1$ and $\beta^* = 1$. ‘DI’ refers to the ‘drag-inertia’ regime, ‘DL’ to the Rayleigh-Plateau regime, ‘SOL’ to the ‘soliton-like’ regime and ‘DG’ to the ‘drag-gravity’ regime.

the experiments by Kliakhandler *et al.* [2] and Duprat *et al.* [4, 5].

We first focused on isolated waves running on a constant thickness substrate, or solitary waves. The dynamics of the film seems to be dominated by these structures even when the flow becomes disordered [2, 3]. We examined in detail, via both asymptotic analysis and through elements from dynamical systems theory, the shape, speed and amplitude of the waves for four fluids of increasing viscosities: Water, Rhodorsil silicon oils v50, v1000 and the castor oil utilised in the experiments by [2].

We identified four distinct regimes corresponding to the competition of the two instability modes, the K and RP modes, prompted by inertia and azimuthal curvature (the fibre curvature effectively), respectively, with the viscous dispersion (i.e. the second-order axial viscous diffusion and second-order viscous contributions to the tangential stress at the free

surface) and with the advection of the structures by the flow, which results from the balance between gravity and viscous drag. Two of these regimes are similar to what is found in the planar geometry [9]. The ‘drag-gravity’ regime corresponds to the predominance of the flow advection over the instability mechanisms, either when inertia effects are weak, i.e. for $\delta \lesssim 1$ or when the azimuthal curvature effects are non-dominant, $\beta^* \lesssim 1$. In both cases it is possible to interpret the ‘drag-gravity’ regime as one where the instability growth is arrested by the flow which determines the amplitude and speed of the solitary waves as reflected by the asymptotic relations (32). The ‘drag-inertia’ regime is observed at large reduced Reynolds numbers, $\delta \gg 1$, when the wave characteristics are determined by the balance of inertia, drag and gravity. We have obtained the asymptotic limit of the speed and showed that the rate of convergence to this limit is governed by $\eta/\delta^2 \propto Re^{-2}$.

The ‘drop-like’ regime corresponding to the predominance of the RP instability mechanism over the flow advection. It is specific to the cylindrical geometry and is observed for small fibre radii R compared to the capillary length l_c , that is at small Goucher numbers Go , when the typical time of growth of the RP instability is greater than the advection time of a wavy structure, i.e. for $\beta^* \gtrsim 1$. The maximum reachable amplitude and speed of the waves in this regime is governed by the radius R of the fibre and the balance of gravity and viscous drag. Comparisons to quasi-static drop solutions of the Laplace–Young equation (B1) sliding down a fibre with a speed verifying the Landau–Levich–Derjaguin law (B4) show excellent agreement, even in the case of spherical drops where the long-wave lubrication assumption does not strictly apply. In this regime, waves have a drop-like nearly symmetrical shape determined by capillary effects. The thickness of the substrate film on which the drops slide is governed by the balance of viscosity and capillarity. ‘Drop-like’ TW solution branches subcritically emerge from the Nusselt uniform film branch. We have given an explanation for this subcritical onset based on geometric and thermodynamic arguments and thus completed its recent investigation in [47]. This phenomenon arises from capillary effects and depends only on the aspect ratio $\tilde{\alpha}$ for sufficiently low Goucher numbers.

We have also found a possible fourth regime for very viscous fluids and thick films ($\tilde{\alpha} = O(1)$), for which both K and RP instability mechanisms are weak ($\delta \lesssim 1$ and $\beta^* \lesssim 1$) and viscous dispersion is significant ($\eta = O(1)$). This ‘soliton-like’ regime corresponds to the balance of the nonlinearities with the dispersion induced by second-order viscous effects, with the speed and amplitude of the solitary waves being functions of the logarithm of the

aspect ratio $\tilde{\alpha}$.

Our study of the solitary-wave solutions has been followed by construction of the TW branches of solutions corresponding to the experimental conditions for which the average flow rate is the true control parameter, with the substrate thickness being determined by the solution itself. If the substrate thickness h_s and the maximum amplitude h_{\max} grow when TWs approach homoclinicity, the ratio of the two, h_{\max}/h_s , evolves in a manner that strongly depends on which instability mechanism is dominant. If the RP instability is dominant, h_{\max}/h_s decreases as the wavenumber k tends to zero, whereas if the K mode is dominant h_{\max}/h_s has an opposite trend. This picture can be even more complex since the predominance of the instability modes can be exchanged by varying the periodicity of the waves and thus the substrate thickness (cf. Fig. 13). The selected wave regime depends not only on the properties of the Nusselt flow at the inlet but also on the periodicity selected by the system. Indeed, the boundaries separating the different regimes are not only functions of Go and $\tilde{\alpha}$ but also functions of the thickness of the substrate, which is determined by the typical distance separating solitary-like waves. Therefore, the phase diagrams displayed in Fig. 17 must be taken with caution. The wave selection process of a noise-driven falling film is the complex result of the linear amplification of inlet perturbations and the downstream nonlinear interaction mechanisms [21, 49, 50].

Noteworthy is that in our previous study on the fibre problem [17], we have shown that the wave selection process of the noise-driven wave dynamics down the fibre is strongly affected by viscous dispersion. This effect is generally weak in the experiments devoted to falling films on planar substrate, where working fluids were often weakly viscous, i.e. water [40, 41, 51]. In the case of films down fibres, the oils used in the experiments are much more viscous than water which explains that viscous dispersion can be dominant and can promote a ‘soliton-like’ regime. In this regime and despite the dissipative nature of the flow, it is possible to observe the formation of solitons, i.e. solitary waves whose shape and speed are not altered by collisions with other solitary waves (such waves are still dissipative but they share several common features with solitons in conservative systems [52]). We explore such effects in Fig. 18 which depicts a simulation of the interaction between two solitons. Chosen parameters correspond to Rhodorsil silicon oil v1000 and $Go = 0.6$. Two pulse-like perturbations of different amplitudes are initially placed in the computational domain (cf. panel a). The excess mass carried by these two perturbations are then drained behind the

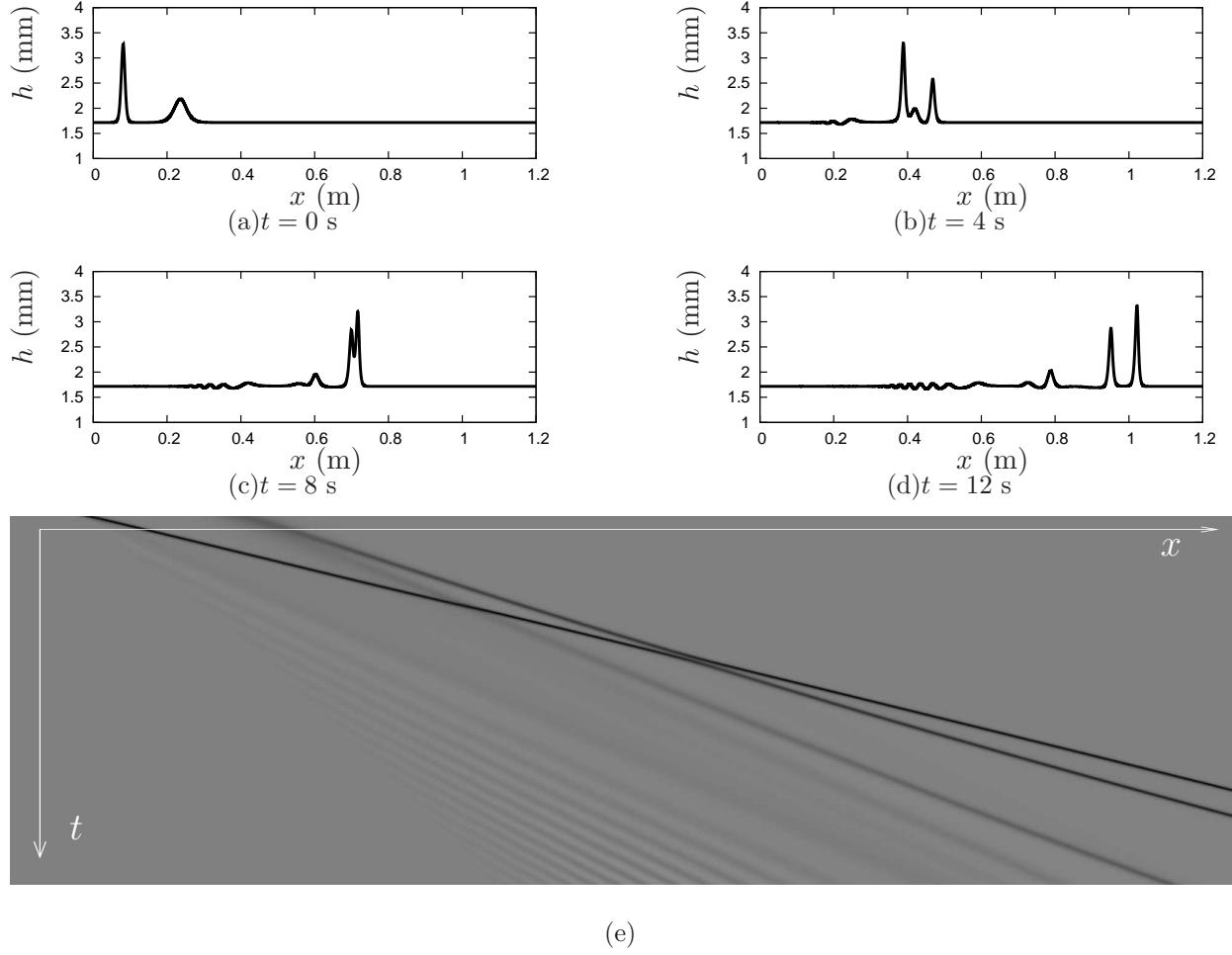


FIG. 18. Simulation of the response of the film in the ‘soliton-like’ regime. Initial conditions consist of two pulse-like perturbations of different amplitudes. Parameters are $\delta = 0.18$, $\tilde{\alpha} = 1.9$ and $\eta = 1.2$ (Rhodorsil silicon oil v1000, $q_N = 300$ mg/s and $R = 0.89$ mm). (a-d) Snapshots of the film thickness at increasing times; (e) Spatio-temporal diagram. Vertical and horizontal ranges are 1.25 m and 28 s respectively. Elevations (depressions) of the free surface are coded in dark (light) grey.

two pulses creating two wave-packets. The spatial extend of these packets grows in time due to the convective instability of the film [4, 17]. Panel b shows the interaction of the second pulse with the mass ejected by the first pulse. The spatio-temporal diagram shown in panel e indicates that the second pulse first overtakes this excess mass and next the first pulse without absorbing them (cf. panels c and d). The coalescence of the two pulses is accompanied by a phase shift but no notable modifications of the speeds and amplitudes

of the pulses as in Hamiltonian systems: The initial wave profiles get superimposed as the waves collide and reappear as the waves move apart. Yet, a slow evolution of the amplitude and speed of the two solitons can be observed towards the speed $c = 7.5$ cm/s and amplitude $h_{\max} = 3.3$ mm of the infinite-domain solitary-wave solution for the given set of parameters.

Our hope is that this new evidence of existence of solitons on a liquid film flowing down a fibre, a dissipative system as opposed to a Hamiltonian one, may motivate a renewed interest for the experimental investigation of the resulting wave dynamics and, in particular, on the role of viscous dispersion.

ACKNOWLEDGMENTS

We acknowledge financial support through a travel grant supported by the Franco-British Alliance Research Partnership Programme and from the Multiflow ITN Marie Curie network funded by the European Commission (GA-2008-214919). The authors thank Imperial College and Laboratoire FAST for hospitality.

Appendix A: Coefficients of the model (3)

The expressions of the coefficients entering the averaged momentum balance (3b) consist of ratios of polynomials in b and $\log(b)$, where $b = 1 + \alpha h$ is the ratio of the total radius

$R + h$ to the fibre radius R :

$$\phi = [3 \left((4 \log(b) - 3)b^4 + 4b^2 - 1 \right)] / [16(b - 1)^3] , \quad (\text{A1a})$$

$$F = 3F_a/[16(b - 1)^2\phi F_b] , \quad (\text{A1b})$$

$$F_a = -301b^8 + 622b^6 - 441b^4 + 4 \log(b) \left\{ 197b^6 - 234b^4 + 6 \log(b) \right. \\ \left. \times [16 \log(b)b^4 - 36b^4 + 22b^2 + 3] b^2 + 78b^2 + 4 \right\} b^2 + 130b^2 - 10 , \quad (\text{A1c})$$

$$F_b = 17b^6 + 12 \log(b) [2 \log(b)b^2 - 3b^2 + 2] b^4 - 30b^4 + 15b^2 - 2 , \quad (\text{A1d})$$

$$G = G_a/[64(b - 1)^4\phi^2 F_b] , \quad (\text{A1e})$$

$$G_a = 9b \left\{ 4 \log(b) [-220b^8 + 456b^6 - 303b^4 + 6 \log(b) (61b^6 - 69b^4 \right. \\ \left. + 4 \log(b) (4 \log(b)b^4 - 12b^4 + 7b^2 + 2) b^2 + 9b^2 + 9) b^2 + 58b^2 + 9] b^2 \right. \\ \left. + (b^2 - 1)^2 (153b^6 - 145b^4 + 53b^2 - 1) \right\} , \quad (\text{A1f})$$

$$I = 64(b - 1)^5\phi^2/[3F_b] , \quad (\text{A1g})$$

$$J = 3J_a/[128(b - 1)^4\phi^2 F_b] , \quad (\text{A1h})$$

$$J_a = 9 \left\{ (490b^8 - 205b^6 - 235b^4 + 73b^2 - 3) (b^2 - 1)^3 \right. \\ \left. + 4b^2 \log(b) [2b^4 \log(b) (72 \log(b) (2 \log(b)b^4 - 6b^4 + b^2 + 6) b^4 \right. \\ \left. + (b - 1)(b + 1) (533b^6 - 109b^4 - 451b^2 + 15)) \right. \\ \left. - 3 (b^2 - 1)^2 (187b^8 - 43b^6 - 134b^4 + 17b^2 + 1) \right] \right\} , \quad (\text{A1i})$$

$$K = 3K_a/[16b^3(b - 1)^2\phi F_b] , \quad (\text{A1j})$$

$$K_a = 4b^4 \log(b) (233b^8 - 360b^6 + 12 \log(b) (12 \log(b)b^4 - 25b^4 + 12b^2 + 9) b^4 \\ + 54b^4 + 88b^2 - 15) - (b^2 - 1)^2 (211b^8 - 134b^6 - 56b^4 + 30b^2 - 3) , \quad (\text{A1k})$$

$$L = L_a/[8b(b - 1)^2\phi F_b] , \quad (\text{A1l})$$

$$L_a = 4b^2 \log(b) \left\{ 6 \log(b) (12 \log(b)b^4 - 23b^4 + 18b^2 + 3) b^4 + (b - 1)(b + 1) \right. \\ \left. \times (95b^6 - 79b^4 - 7b^2 + 3) \right\} - (b^2 - 1)^2 (82b^6 - 77b^4 + 4b^2 + 3) , \quad (\text{A1m})$$

$$M = 3 + [24 \log(b)b^8 - 25b^8 + 48b^6 - 36b^4 + 16b^2 - 3] / [2b^2 F_b] . \quad (\text{A1n})$$

We note that in Appendix B in [17] a small misprint can be found in the definition of the factor J —a missing factor of three— that is here corrected.

Appendix B: Static drops on coated fibres: Computations and asymptotic analysis

The shape of an axisymmetric drop sitting on a vertical fibre has been computed numerically by Kumar and Hartland [53] and determined analytically by Carroll [54] by neglecting gravity effects. When the contact angle of the liquid with the solid fibre vanishes, the analytical solution corresponds to an unduloid [7, 55] that can be written parametrically using elliptic integrals of the first and second kind. However, the analytical solution is cumbersome to use and requires numerical evaluation of the different integrals involved. Hence, we choose to determine the solution by solving numerically the Laplace–Young equation parametrically rewritten as [53]:

$$\frac{d\phi}{d\tilde{s}} = \left(\frac{d\phi}{d\tilde{s}} \right)_t + \frac{1}{R_t} - \frac{\sin \phi}{\tilde{r}}, \quad (\text{B1a})$$

$$\frac{d\tilde{r}}{d\tilde{s}} = \cos \phi, \quad \text{and} \quad \frac{d\tilde{x}}{d\tilde{s}} = \sin \phi, \quad (\text{B1b})$$

where the length scale is the fibre radius, \bar{R} . The radial and axial coordinates are denoted by \tilde{r} and \tilde{x} , respectively. \tilde{s} denotes the curvilinear arc length along the drop interface whereas ϕ is the angular inclination of the drop interface to the radial axis whereas $(d\phi/ds)_t + 1/R_t$ denotes the mean curvature at the top of the drop, $s = 0$. The set of equations is completed by the boundary conditions:

$$\phi = \pi/2, \quad \tilde{r} = R_t, \quad \tilde{x} = 0, \quad \text{at} \quad \tilde{s} = 0. \quad (\text{B1c})$$

The contact area \tilde{A} separating the liquid and gas phases and the volume \tilde{V} of the drop has been computed by solving:

$$\frac{d\tilde{A}}{d\tilde{s}} = 2\pi\tilde{r} \quad \text{and} \quad \frac{d\tilde{V}}{d\tilde{s}} = \pi(\tilde{r}^2 - R_t^2) \quad (\text{B1d})$$

We have solved system (B1) using the AUTO07P software [30]. We have adjusted R_t to the coated fibre radius $1 + \tilde{\alpha}$, and the drop volume V to the volume of the corresponding solitary wave, after subtracting the volume of the residual film.

The speed of the quasi-static drops sliding on a vertical fibre can be estimated using the Landau-Levich-Derjaguin theory [56, 57]. For this purpose we divide a large amplitude sliding drop in two separate regions. The ‘inner’ one corresponding to the thin films at the upper and lower ends of the drop where viscosity balances capillary forces, and the ‘outer’ one, the quasi-static drop itself which is governed by the Laplace–Young equation given

above. In the inner region, $h \ll R$ and the equation to be solved reduces to (6), whose TW solutions are governed by:

$$\frac{h^3}{3}(1 + \beta h' + h''') - c(h - 1) - 1 = 0 \quad (\text{B2})$$

Following [13], we introduce the inner coordinates $X = c^{-1/3}\xi$ where $c \gg 1$ and get to leading order

$$h''' = 3(h - 1)/h^3 \quad (\text{B3})$$

which is the so-called ‘Bretherton equation’ [13, 58], originating from Bretherton’s work on the motion of a long gas bubble in a capillary tube. In the upper region, the solution of the Bretherton equation with boundary conditions $h = 1$, $h' = h'' = 0$ at $X = 0$ is monotonic. The numerical solution of (B3) yields $\lim_{X \rightarrow \infty} h'' = 1.34$. The speed of the drops is then selected by asymptotically matching the solutions of (B1) and (B3) in the upper overlap region between inner and outer domains. This can be easily done by imposing that the Laplace pressures corresponding to the two solutions are equal in this region giving:

$$\left(\frac{d\phi}{d\tilde{s}}\right)_t + \frac{1}{R_t} = 1 + 1.34 \frac{Ca^{2/3}}{\tilde{\alpha}}, \quad (\text{B4})$$

where $Ca = c_{\text{drops}} Bo = \mu \bar{c}_{\text{drops}}/\sigma$ in the limit $\tilde{\alpha} \ll 1$.

-
- [1] D. Quéré, *Europhys. Lett.* **13**, 721 (1990).
 - [2] I. L. Kliakhandler, S. H. Davis, and S. G. Bankoff, *J. Fluid Mech.* **429**, 381 (2001).
 - [3] R. V. Craster and O. K. Matar, *J. Fluid Mech.* **553**, 85 (2006).
 - [4] C. Duprat, C. Ruyer-Quil, S. Kalliadasis, and F. Giorgiutti-Dauphiné, *Phys. Rev. Lett.* **98**, 244502 (2007).
 - [5] C. Duprat, C. Ruyer-Quil, and F. Giorgiutti-Dauphiné, *Phys. Fluids* **21**, 042109 (2009).
 - [6] P. L. Kapitza and S. P. Kapitza, in *Collected papers of P. L. Kapitza (1965)*, edited by D. T. Haar (Pergamon (Oxford), 1949) pp. 690–709, (Original paper in Russian: *Zh. Ekper. Teor. Fiz.* **19**, 105–120).
 - [7] J. Plateau, *Statique Expérimentale et Théorique des Liquides Soumis aux seules Forces Moléculaires* (Gauthier Villars Paris, 1873).
 - [8] L. Rayleigh, *Proc. Lond. Math. Soc.* **10**, 4 (1878).

- [9] T. Ooshida, Phys. Fluids **11**, 3247 (1999).
- [10] C. Ruyer-Quil and P. Manneville, J. Fluid Mech. **531**, 181 (2005).
- [11] A. Frenkel, Europhys. Lett. **18**, 583 (1992).
- [12] Y. Y. Trifonov, AIChE J. **38**, 821 (1992).
- [13] S. Kalliadasis and H.-C. Chang, J. Fluid Mech. **261**, 135 (1994).
- [14] R. V. Roy, A. J. Roberts, and A. J. Simpson, J. Fluid Mech. **454**, 235 (2002).
- [15] A. J. Roberts and Z. Li, J. Fluid Mech. **553**, 33 (2006).
- [16] E. Novbari and A. Oron, Phys. Fluids **21**, 062107 (2009).
- [17] C. Ruyer-Quil, P. Treveleyan, F. Giorgiutti-Dauphiné, C. Duprat, and S. Kalliadasis, J. Fluid Mech. **603**, 431 (2008).
- [18] A. Oron, O. Gottlieb, and E. Novbari, Eur. J. Mech. B/Fluids **28**, 1 (2009).
- [19] Following the terminology introduced in [22–24], a film flow model is *consistent* at $O(\epsilon^n)$ when all neglected terms are of higher order, or equivalently no terms of $O(\epsilon^n)$ or smaller have been omitted, and hence a gradient expansion of the model up to $O(\epsilon^n)$ agrees exactly with the single evolution equation for h at $O(\epsilon^n)$ obtained with just the long-wave approximation.
- [20] C. Duprat, F. Giorgiutti-Dauphiné, D. Tseluiko, S. Saprykin, and S. Kalliadasis, Phys. Rev. Lett. **103**, 234501 (2009).
- [21] M. Pradas, D. Tseluiko, and S. Kalliadasis, Phys. Fluids **23**, 044104 (2011).
- [22] C. Ruyer-Quil and P. Manneville, Eur. Phys. J. B **6**, 277 (1998).
- [23] C. Ruyer-Quil and P. Manneville, Eur. Phys. J. B **15**, 357 (2000).
- [24] C. Ruyer-Quil and P. Manneville, Phys. Fluids **14**, 170 (2002).
- [25] D. Quéré, Annu. Rev. Fluid Mech. **31**, 347 (1999).
- [26] V. Ya. Shkadov, Izv. Ak. Nauk SSSR, Mekh. Zhidk Gaza **1**, 63 (1977).
- [27] G. M. Sisoiev, R. V. Craster, O. K. Matar, and S. V. Gerasimov, Chem. Eng. Sci. **61**, 7279 (2006).
- [28] H.-C. Chang and E. A. Demekhin, J. Fluid Mech. **380**, 233 (1999).
- [29] A. Pumir, P. Manneville, and Y. Pomeau, J. Fluid Mech. **135**, 27 (1983).
- [30] E. Doedel, A. R. Champneys, T. F. Fairgrieve, Y. A. Kuznetsov, B. Sandstede, and X.-J. Wang, AUTO97: *Continuation and bifurcation software for ordinary differential equations*, Tech. Rep. (Department of Computer Science, Concordia University, Montreal, Canada, 1997) (Available by FTP from `ftp.cs.concordia.ca` in directory `pub/doedel/auto`).

- [31] Even though, strictly speaking δ is not allowed to tend to infinity, the question of the behaviour of different quantities of interest for large δ is a valid one within the context of the WRIBL model as model equations.
- [32] S. D. R. Wilson, *J. Engng Maths* **16**, 209 (1982).
- [33] H. A. Thomas, in *Proc. Hydraulics Conf.* (Univ. of Iowa, 1939) pp. 214–229.
- [34] Q. Q. Liu, L. Chen, J. C. Li, and V. P. Singh, *J. Hydrologic Engng.* **10**, 110 (2005).
- [35] T. Kawahara, *Phys. Rev. Lett.* **51**, 381 (1983).
- [36] T. Kawahara and S. Toh, *Phys. Fluids* **31**, 2103 (1988).
- [37] D. Tseluiko, S. Saprykin, and S. Kalliadasis, *Proc. Est. Acad. Sci.* **59**, 139 (2010).
- [38] D. Tseluiko, S. Saprykin, C. Duprat, F. Giorgiutti-Dauphiné, and S. Kalliadasis, *Physica D* **239** (2010).
- [39] H.-C. Chang, *Phys. Fluids* **29**, 3142 (1986).
- [40] J. Tihon, K. Serif, K. Argyriadi, and V. Bontozoglou, *Experiments in Fluids* **41**, 79 (2006).
- [41] J. Liu and J. P. Gollub, *Phys. Fluids* **6**, 1702 (1994).
- [42] B. Scheid, C. Ruyer-Quil, U. Thiele, O. A. Kabov, J. C. Legros, and P. Colinet, *J. Fluid Mech.* **527**, 303 (2005).
- [43] H.-C. Chang, E. A. Demekhin, and D. I. Kopelevitch, *J. Fluid Mech.* **250**, 433 (1993).
- [44] H.-C. Chang and E. A. Demekhin, *Complex Wave Dynamics on Thin Films* (D. Möbius and R. Miller, Elsevier, 2002).
- [45] C. Ruyer-Quil, *Dynamique d'un film mince s'écoulant le long d'un plan incliné*, Ph.D. thesis, École polytechnique, LadHyx, France (1999).
- [46] S. V. Alekseenko, V. E. Nakoryakov, and B. G. Pokusaev, *Wave Flow in Liquid Films*, 3rd ed. (Begell House (New York), 1994).
- [47] E. Novbari and A. Oron, *Phys. Fluids* **23**, 012105 (2011).
- [48] Indeed, Kapitza himself erroneously predicted the instability threshold of a falling film using thermodynamic arguments [59], a question that was settled with Benjamin's work a few years later [60].
- [49] H.-C. Chang, E. Demekhin, and E. Kalaidin, *J. Fluid Mech.* **294**, 123 (1995).
- [50] S. Kalliadasis and U. Thiele, *Thin Films of Soft Matter* (Springer-CISM (Wien), 2007).
- [51] S. V. Alekseenko, V. Y. Nakoryakov, and B. G. Pokusaev, *AIChE J.* **31**, 1446 (1985).
- [52] C. I. Christov and M. G. Velarde, *Physica D* **86**, 323 (1995).

- [53] A. Kumar and S. Hartland, J. Colloid Interface Sci. **124**, 67 (1988).
- [54] B. J. Carroll, J. Colloid Interface Sci. **57**, 488 (1976).
- [55] C. Delaunay, J. Math. Pures et Appliquées **6**, 309 (1841).
- [56] L. D. Landau and B. V. Levich, Acta Physicochim. **17**, 42 (1942).
- [57] B. V. Derjaguin, Acta Physicochim. URSS **39**, 13 (1943).
- [58] F. P. Bretherton, J. Fluid Mech. **10**, 166 (1961).
- [59] P. L. Kapitza, in *Collected papers of P. L. Kapitza (1965)*, edited by D. T. Haar (Pergamon (Oxford), 1948) pp. 662–689, (Original paper in Russian: Zh. Ekper. Teor. Fiz. **18**, I. 3–18, II. 19–28).
- [60] T. B. Benjamin, J. Fluid Mech. **2**, 554 (1957), corrigendum, 3:657.